The Astrophysical Journal, 927:49 (24pp), 2022 March 1 https://doi.org/10.3847/1538-4357/ac400d

A Comparison of Multiphase Magnetic Field Tracers in a High Galactic Latitude Region of the Filamentary Interstellar Medium

J. L. Campbell[1,2], S. E. Clark[3,4], B. M. Gaensler[1,2], A. Marchal[5], C. L. Van Eck[2], A. A. Deshpande[6,7], S. J. George[8], S. J. Gibson[9], R. Ricci[10], J. M. Stil[11], and A. R. Taylor[12,13]
[1] David A. Dunlap Department of Astronomy & Astrophysics, University of Toronto, 50 St. George St., Toronto, ON M5S 3H4, Canada; campbell@astro.utoronto.ca
[2] Dunlap Institute for Astronomy and Astrophysics, University of Toronto, 50 St. George St., Toronto, ON M5S 3H4, Canada
[3] Department of Physics, Stanford University, Stanford, CA 94305, USA
[4] Kavli Institute for Particle Astrophysics & Cosmology, P.O. Box 2450, Stanford University, Stanford, CA 94305, USA
[5] Canadian Institute for Theoretical Astrophysics, University of Toronto, 60 St. George St., Toronto, ON M5S 3H8, Canada
[6] Inter-University Centre for Astronomy and Astrophysics, Pune 411007, India
[7] Indian Institute of Technology, Kanpur 208016, India
[8] School of Physics & Astronomy, University of Birmingham, B15 2TT, UK
[9] Department of Physics & Astronomy, Western Kentucky University, 1906 College Heights Blvd., Bowling Green, KY 42101, USA
[10] Istituto Nazionale di Ricerche Metrologiche, strada delle cacce 91, ZIP code I-10135 Torino, Italy
[11] Department of Physics and Astronomy, The University of Calgary, 2500 University Drive NW, Calgary AB T2N 1N4, Canada
[12] Inter-University Institute for Data Intensive Astronomy, and Department of Astronomy, University of Cape Town, Republic of South Africa
[13] Department of Physics and Astronomy, University of the Western Cape, Republic of South Africa
Received 2021 June 18; revised 2021 November 30; accepted 2021 December 2; published 2022 March 3

Abstract

Understanding how the Galactic magnetic field threads the multiphase interstellar medium (ISM) remains a considerable challenge, as different magnetic field tracers probe dissimilar phases and field components. We search for evidence of a common magnetic field shared between the ionized and neutral ISM by comparing 1.4 GHz radio continuum polarization and H I line emission from the Galactic Arecibo *L*-Band Feed Array Continuum Transit Survey (GALFACTS) and Galactic Arecibo *L*-Band Feed Array H I (GALFA-H I) survey, respectively. We compute the polarization gradient of the continuum emission and search for associations with diffuse/translucent H I structures. The polarization gradient is sensitive to changes in the integrated product of the thermal electron density and line-of-sight field strength ($B_{\parallel}$) in warm ionized gas, while narrow H I structures highlight the plane-of-sky field orientation in cold neutral gas. We identified one region in the high Galactic latitude Arecibo sky, G216 +26 centered on (ℓ, b) ∼ (216°, +26°), containing filaments in the polarization gradient that are aligned with narrow H I structures roughly parallel to the Galactic plane. We present a comparison of multiphase observations and magnetic field tracers of this region, demonstrating that the warm ionized and cold neutral media are connected likely via a common magnetic field. We quantify the physical properties of a polarization gradient filament associated with Hα emission, measuring a line-of-sight field strength $B_{\parallel} = 6 \pm 4\ \mu$G and a plasma beta $\beta = 2.1^{+3.1}_{-2.1}$. We discuss the lack of widespread multiphase magnetic field alignments and consider whether this region is associated with a short-timescale or physically rare phenomenon. This work highlights the utility of multitracer analyses for understanding the magnetized ISM.

Unified Astronomy Thesaurus concepts: Astrophysical magnetism (102); Milky Way magnetic fields (1057); Interstellar medium (847); Interstellar magnetic fields (845); Interstellar filaments (842); Interstellar phases (850)

1. Introduction

The diffuse interstellar medium (ISM) of our Galaxy is a complex multiphase environment threaded with magnetic fields. This Galactic magnetic field (GMF) plays a crucial role in many astrophysical processes that drive Galactic evolution. Yet, despite its significance in a variety of Galactic environments, a complete understanding of the GMF has been substantially hampered by the difficulty in interpreting its three-dimensional (3D) multiphase geometry (Haverkorn et al. 2019; Jaffe 2019). This challenge is largely due to the observational limitation that various magnetic field tracers probe the GMF in different phases of the ISM, while also providing only one- or two-dimensional projections of its full vector morphology (see Jaffe 2019; Ferrière 2020, for overviews on magnetic field tracers). As a result, understanding how the GMF is structured between different ISM phases remains poorly understood.

The ISM phases can be broadly categorized into ionized, atomic, and molecular and have a range of temperatures and densities (see Ferrière 2001). A primary component of the ionized ISM is the warm ionized medium (WIM), sometimes referred to as diffuse ionized gas (DIG) in other galaxies (Haffner et al. 2009). The WIM has a typical gas temperature $T \sim 10^4$ K and volume-averaged thermal electron density $n_e \sim 0.01$–$0.1\ \mathrm{cm}^{-3}$ (Reynolds 1990a; Weisberg et al. 2008) and pervades much of the Galactic volume. Galactic maps of Hα emission reveal many filaments, loops, and bubbles superimposed on a diffuse background that is often considered to be the WIM. The ultraviolet radiation from massive OB stars within the Galactic midplane is believed to sustain the ionization of the WIM (Reynolds 1984, 1990c; Haffner et al. 2009; Kado-Fong et al. 2020), although there remain questions as to how this radiation percolates through the ISM to maintain the ionization at high Galactic latitudes (e.g., Reynolds 1990b; Haffner et al. 2009; Wood et al. 2010; Kim & Ostriker 2018).

The polarized radio sky contains complex features with no corresponding total intensity structures (Wieringa et al. 1993; Gray et al. 1998; Gaensler et al. 2001, 2011). When background polarized radio synchrotron emission passes through the foreground magnetized WIM, birefringence induces a rotation of the incident polarization angle, an effect called Faraday rotation. This process is quantified by the rotation measure (RM) and is proportional to the product of the thermal electron density (n_e) and line-of-sight (LOS) magnetic field strength ($B_\parallel$) integrated along the LOS. Faraday rotation alone cannot disentangle the degeneracy between n_e and $B_\parallel$ and provides no information about either of their LOS distributions (Ferrière 2016).

The polarization gradient ($|\boldsymbol{\nabla P}|_{\rm max}$) is a spatial gradient of the complex polarization vector $Pe^{2i\chi}$, where P is the polarized intensity and χ is the polarization angle, revealing a network of small-scale filaments interpreted as turbulent-driven fluctuations in n_e and/or $B_\parallel$ (Gaensler et al. 2011). Much larger features in the polarization gradient have been shown to be associated with the edges of supernova remnants and H II regions (e.g., Iacobelli et al. 2014). In the diffuse ISM, Faraday rotation primarily traces the WIM (e.g., Haverkorn et al. 2004a, 2004b; Hill et al. 2008; Gaensler et al. 2011; Heiles & Haverkorn 2012). Work by Thomson et al. (2019) has evoked some debate over whether significant Faraday rotation may occur within predominantly neutral regions with increased magnetic field strengths (Bracco et al. 2020). There is also evidence that Faraday rotation may occur within molecular clouds (Tahani et al. 2018).

The neutral atomic medium exists in two thermally stable phases: the dense cold neutral medium (CNM) and the more rarefied warm neutral medium (WNM). The CNM ($T \sim 10$–100 K, $N_{\rm HI} \sim 7$–$70\,{\rm cm}^{-3}$; McKee & Ostriker 1977; Wolfire et al. 2003) is often structured into sheets and filaments, occupying a small fraction of the Galactic volume (Heiles 1967; Heiles & Troland 2003; Verschuur 1970; Clark et al. 2014), while the WNM ($T \sim 10^4$ K, $N_{\rm HI} \sim 0.2$–$0.9\,{\rm cm}^{-3}$; McKee & Ostriker 1977; Wolfire et al. 2003; Marchal & Miville-Deschênes 2021) is more extended and fills a larger Galactic volume (Heiles & Troland 2003). The CNM and WNM coexist in mutual pressure equilibrium (Field et al. 1969; Goldsmith et al. 1969). There also exists a thermally unstable neutral medium (UNM) within which a significant fraction of H I gas has been shown to exist (Heiles & Troland 2003; Kanekar et al. 2003; Roy et al. 2013; Saury et al. 2014; Murray et al. 2015, 2018; Marchal & Miville-Deschênes 2021). Of the total H I mass, it is believed that ∼30% is in the CNM phase and ∼50% is in the WNM phase, with the remaining ∼20% occupying the thermally unstable regime (Murray et al. 2018).

Velocity-resolved H I data reveal long, narrow structures deemed "H I fibers" at high Galactic latitude that are very well aligned with the plane-of-sky (POS) magnetic field orientation traced using starlight (Clark et al. 2014) and dust polarization data (Clark et al. 2015; Martin et al. 2015; Kalberla et al. 2016; Blagrave et al. 2017). While some authors have interpreted these H I structures as velocity caustics imprinted by the turbulent velocity field (Lazarian & Yuen 2018), a number of observational measurements have instead shown that they are real density structures residing in the cold ISM. Such evidence includes ratios of far-infrared to H I column density (Clark et al. 2019), NaI absorption profile equivalent widths (Peek & Clark 2019), and column density power spectra (Kalberla & Haud 2020).

Observational studies that provide evidence for magnetic field alignments between the ionized and neutral medium are sparse. The first of these was the 3C 196 LOFAR (van Haarlem et al. 2013) field containing strong spatial alignments between radio polarized intensity structures, the POS magnetic field orientation in Planck dust polarization data, and linear depolarization canals (Jelić et al. 2015; Zaroubi et al. 2015; Jelić et al. 2018; Turić et al. 2021), as well as H I filaments (Kalberla & Kerp 2016). These morphological alignments led the authors to conclude that the magnetized ionized and neutral media are clearly connected and that the regular magnetic field plays an important role in confining these phases of the diffuse ISM. The Horologium and Auriga fields located within the Fan Region (van de Hulst 1967; Wolleben et al. 2006), a strongly polarized Galactic structure (Hill et al. 2017), were subsequently shown to exhibit an alignment between depolarization canals (Haverkorn et al. 2003a, 2003b) and H I filaments (Kalberla et al. 2017). The authors again attributed this morphological alignment to the local magnetic field confining the magnetized ionized and neutral ISM together, suggesting that the ionized medium associated with the radio polarized filament is likely wrapped around the filamentary H I emission.

Despite the spatial correlations found across the multiphased and magnetized ISM, such comparisons are often challenging and difficult to interpret (Haverkorn et al. 2019; Jaffe 2019). It thus remains unclear whether the local magnetic field is shared between the Faraday-rotating plasma and filamentary neutral medium in these regions and, if so, how the GMF is morphologically connected between them. Further studies are required to understand whether such regions are representative of the mean magnetic field of the Milky Way and our ability to identify them is observationally limited, or if they are somehow unique locations in the Galaxy.

In this work, we search for evidence that the GMF is shared between the warm ionized and cold neutral ISM using radio polarization gradients and H I structures in Arecibo data. The structure of this paper is as follows. An overview of the data is presented in Section 2, followed by our multiphase results and the key morphological structures described in Section 3. Our comparison of polarization gradient and H I structures is presented in Section 4, and key astrophysical quantities are computed in Section 5. Our discussion is presented in Section 6. Our summary and conclusions are given in Section 7.

2. Data Overview

2.1. 1.4 GHz Radio Polarization

We use radio polarization data from Data Release (DR) 3.1.2 of the Galactic Arecibo *L*-Band Feed Array Continuum Transit Survey (GALFACTS), a spectropolarimetric sky survey (Taylor & Salter 2010) that provides wide-field high-resolution Stokes maps of $I_{1.4}$, $Q_{1.4}$, $U_{1.4}$, and $V_{1.4}$, where the subscripts refer to the 1.4 GHz frequency. The primary science goal of GALFACTS is to advance our understanding of the magnetoionic properties of the Milky Way by mapping the radio polarized sky and deriving key polarization properties for both discrete point sources and the diffuse ISM. The data have an angular resolution of $3\farcm5$ (Taylor & Salter 2010). The full data will cover a ∼300 MHz (1214–1525 MHz) bandwidth but are currently limited to a ∼160 MHz (1367–1525 MHz) bandwidth across 376 binned spectral channels. The observations were

taken throughout the period of 2008–2016 with the 305 m single-dish William E. Gordon (Arecibo) telescope in Puerto Rico using the Arecibo L-band feed array (ALFA). GALFACTS offers complete sky coverage of ∼12,700 deg^2 within the decl. range of $-0.^\circ 8 < \delta < +37.^\circ 8$. The data consist of a north survey (with fields N[1−4]), south survey (S[1−4]), and zenith survey (Z[1−4]), with each resulting data cube covering $512' \times 512'$ ($8.^\circ 53 \times 8.^\circ 53$) on the sky with $1' \times 1'$ pixels (Guram & Taylor 2009; Taylor & Salter 2010). See Guram & Taylor (2009), Guram et al. (2011), and Taylor (2012, 2013) for details on GALFACTS data processing.

The Arecibo data are affected by leakage-related scanning artifacts. As the telescope nods along the meridian, Earth's rotation causes a zig-zag basket-weaving scanning pattern that results in systematic linear artifacts. While post-processing removed most of the scanning artifacts (Guram & Taylor 2009), they are still apparent in the data and become enhanced in the polarization gradient. There are additional artifacts that appear as clusters of short streaks along the scanning direction from intermittent broadband radio frequency interference (RFI; Leahy 2018). To minimize these artifacts in the GALFACTS data, we applied a Fourier destriping technique where artifacts are localized and removed in the Fourier domain (Schlegel et al. 1998) using the SCIPY `fftpack` package (Virtanen et al. 2020) to compute the Fourier transform.

We used a high Galactic latitude noise-dominated region in the S1 footprint to locate the scanning artifacts in Fourier space. The destriping process caused additional artifacts toward bright polarized point sources, so we masked them using a cubic-spline interpolation before proceeding with destriping. This process was effective in minimizing the artifacts in $Q_{1.4}$ and $U_{1.4}$ but does not significantly improve $I_{1.4}$, so we only destripe the polarization data. The final destriped Stokes maps were smoothed to an angular resolution of $5'$ to increase the polarization gradient signal-to-noise ratio (S/N).

The maximum amplitude of the polarization gradient $|\boldsymbol{\nabla P}|_{\rm max}$, sometimes referred to as the generalized polarization gradient, describes the general case in which both P and χ are changing across the image plane (Herron et al. 2018). This differs from the original form of the polarization gradient, where they are assumed to be changing in the same direction (Gaensler et al. 2011). The amplitude of $|\boldsymbol{\nabla P}|_{\rm max}$ is given by

$$|\boldsymbol{\nabla P}_{\rm max}| = \left(\frac{1}{2}\left[\left(\frac{\partial Q}{\partial x}\right)^2 + \left(\frac{\partial U}{\partial x}\right)^2 + \left(\frac{\partial Q}{\partial y}\right)^2 + \left(\frac{\partial U}{\partial y}\right)^2\right] + \frac{1}{2}\sqrt{\left[\left(\frac{\partial Q}{\partial x}\right)^2 + \left(\frac{\partial U}{\partial x}\right)^2 + \left(\frac{\partial Q}{\partial y}\right)^2 + \left(\frac{\partial U}{\partial y}\right)^2\right]^2 - 4\left[\frac{\partial Q}{\partial x}\frac{\partial U}{\partial y} - \frac{\partial Q}{\partial y}\frac{\partial U}{\partial x}\right]^2}\right)^{1/2}, \quad (1)$$

where x and y are Cartesian pixel coordinates of the image and Q and U are the Stokes maps.

The polarization gradient is most sensitive to small-scale structures and can be used as an edge detector to identify sharp changes in the amplitude and/or direction of the complex polarization vector. Due to its sensitivity to small-scale structures, the polarization gradient enhances noise in the image (Burkhart et al. 2012). Convolving Q and U with a Gaussian kernel before computing the spatial gradient is mathematically equivalent to applying a spatial filter to the gradient operator (Robitaille & Scaife 2015). Smoothing the Stokes maps thus increases the S/N while simultaneously probing larger spatial scales in the polarization gradient.

2.2. 21 cm Line Emission

We use velocity-resolved DR 2 Galactic Arecibo *L*-Band Feed Array H I (GALFA-H I) survey H I data (Peek et al. 2018). The GALFA-H I data were commensally observed with GALFACTS using Arecibo and have the same sky coverage and angular resolution. We use custom data cubes with the same sky coverage as the GALFACTS footprints over the velocity range $|v_{\rm lsr}| \leqslant 188$ km s^{-1} with a degraded 0.8 km s^{-1} velocity resolution. The scanning artifacts are not prominent in the H I data and do not significantly affect our analysis, so we do not destripe or smooth the GALFA-H I data.

2.3. Hα Emission

We use the composite Hα map (Finkbeiner 2003) that combines data from the Virginia Tech Spectral line Survey (VTSS; Dennison et al. 1998), Southern H-Alpha Sky Survey Atlas (SHASSA; Gaustad et al. 2001), and Wisconsin H-Alpha Mapper (WHAM; Haffner et al. 2003). The composite data were reprocessed to remove image artifacts, calibrated to a stable zero-point on 1° scales using WHAM, and were resampled to a common $6'$ angular resolution (Finkbeiner 2003).

We complement the composite Hα map with the velocity-resolved WHAM data that have an angular resolution of 1°, velocity resolution of 12 km s^{-1}, and a sensitivity to faint emission on large angular scales (Haffner et al. 2003). This combination of Hα data helps to provide a more complete picture of ionized gas.

2.4. Dust Emission

We use the $5'$ R2.00 Planck 353 GHz Stokes I_{353} all-sky dust map, where the subscript refers to the 353 GHz frequency. The data were post-processed with the Generalized Needlet Internal Linear Combination (`GNILC`) algorithm to remove the cosmic infrared background (CIB) anisotropies from the thermal dust emission (Planck Collaboration et al. 2014). The High Frequency Instrument is calibrated to the cosmic microwave background (CMB) dipole and is measured as a temperature differential in units of K_{CMB}^{-1}. We converted this to units of MJy sr^{-1} via the conversion factor of 287 MJy sr^{-1} K_{CMB}^{-1} (Planck Collaboration et al. 2020a). We subtracted the CIB monopole from the I_{353} map, which has an intensity of 0.13 MJy sr^{-1} at 353 GHz (Planck Collaboration et al. 2020a), and added a Galactic H I offset correction to the I_{353} map of 0.01035 MJy sr^{-1} (Planck Collaboration et al. 2020b).

We complement the I_{353} map with the $80'$ R3.00 Planck Q_{353} and U_{353} dust polarization data (Planck Collaboration et al. 2020a) that were also post-processed with `GNILC`. We subtracted the CMB monopole from Q_{353} and U_{353}, which has an intensity of 0.64 MJy sr^{-1} at this frequency in polarization (Planck Collaboration et al. 2016). The Q_{353} and U_{353} maps follow the COSMO polarization angle convention (Planck Collaboration et al. 2020a), so we converted the data to IAU convention[14] by multiplying U_{353} by −1.

3. Multifrequency Morphology Results

We visually compared structures in the GALFACTS polarization gradient and GALFA-H I emission of the Arecibo sky, focusing on high-Galactic-latitude structures that are

[14] https://www.iau.org/news/announcements/detail/ann16004/

associated with diffuse/translucent H I emission and that are not spatially correlated with excess synchrotron emission. Our search identified G216+26 (hereafter G216) centered on (ℓ, b) $\sim$ (216°, + 26°) as the only region found to contain coherent filaments in the polarization gradient that are spatially correlated with linear H I structures, alluding to a possible connection between their magnetic fields. The remainder of this paper investigates whether the warm ionized ISM and cold neutral ISM are associated in this region and whether they share a common magnetic field.

3.1. 1.4 GHz Synchrotron Emission

Figure 1 shows the 1.4 GHz GALFACTS spectropolarimetry results smoothed to 5′ angular resolution. This includes $I_{1.4}$ (top left), $P_{1.4}$ (middle left), $Q_{1.4}$ (top right), $U_{1.4}$ (middle right), and $|\boldsymbol{\nabla P}|_{\max}$ (bottom center). Recall that several bright polarized point sources were masked and interpolated to prevent additional artifacts in the polarization gradient. Smoothing the destriped $Q_{1.4}$ and $U_{1.4}$ maps from an angular resolution of 3.′5 to 5′ before computing the gradient enhances the S/N in the polarization gradient by a factor of $\gtrsim$2 while retaining most high spatial frequencies.

This region contains two distinct filamentary structures in the polarization gradient that are separated by ∼2°–3°, extend ∼10° in length, and are roughly parallel to the Galactic plane. There is very little indication of the polarization gradient filaments using the 3.′5 resolution data; smoothing $Q_{1.4}$ and $U_{1.4}$ to enhance the S/N allows them to become visible. There is also a "background" of small-scale structures in the polarization gradient that likely reflects noise, unmasked point sources, and discontinuities in n_e and/or $B_{\parallel}$.

The polarization gradient filament farthest from the Galactic plane (F1) is a relatively simple structure that contains a knee-shaped bend (F1K) toward the southern end. The F1K portion of F1 exhibits a clear double-jump morphology (i.e., two parallel filamentary structures). Double-jump morphologies in the polarization gradient have been attributed to a delta or top-hat profile in n_e or $B_{\parallel}$ from strong shocks (Burkhart et al. 2012). South of F1K, the filament extends into a V-shape structure (F1V) where the filament breaks off into two filamentary structures. While F1V is poorly seen in the 5′ resolution polarization gradient, it can be seen in the Stokes maps and, with significantly greater levels of smoothing, is observed at lower-resolution maps of the polarization gradient. Further smoothing does not significantly change the polarization gradient map.

The polarization gradient filament closer to the Galactic plane (F2) is more complex than F1, containing three filaments toward the north (F2N) and two filaments toward the south (F2S). While F2S contains a double-jump feature, one of these filaments is straight while the other is slightly curved, unlike the F1K parallel double-jump morphology. The F2N triple-jump morphology comprises three unequal-length parallel filaments.

The $I_{1.4}$ data contain background extragalactic point sources in addition to broad vertical and horizontal features from a combination of scanning artifacts and quasi-stationary RFI (Leahy 2018). As defined by our search criteria, we find no spatial correlation between $I_{1.4}$ and the structures described here.

3.2. 21 cm H I Emission

Figure 2 shows integrated column density maps of the velocity-resolved GALFA-H I data across the full velocity range that contains emission, calculated from the brightness temperature maps under the optically thin assumption

$$N_{\rm H\,I} = 1.823 \times 10^{18}\,{\rm cm^{-2}} \int \left(\frac{T_B}{\rm K}\right)\left(\frac{dv_{\rm lsr}}{\rm km\ s^{-1}}\right), \qquad (2)$$

a reasonable assumption to make at these latitudes (Murray et al. 2018). The H I data have been integrated over $-30\ {\rm km\ s^{-1}} \leqslant v_{\rm lsr} \leqslant -10\ {\rm km\ s^{-1}}$ (top left), $-10\ {\rm km\ s^{-1}} \leqslant v_{\rm lsr} \leqslant +4\ {\rm km\ s^{-1}}$ (top right), $+4\ {\rm km\ s^{-1}} \leqslant v_{\rm lsr} \leqslant +20\ {\rm km\ s^{-1}}$ (bottom left), and $+20\ {\rm km\ s^{-1}} \leqslant v_{\rm lsr} \leqslant +40\ {\rm km\ s^{-1}}$ (bottom right) to show various features in the data.

At more negative velocities (Figure 2, top left) the H I emission is localized to the northeast corner ($N_{\rm HI} \sim 3.5 \times 10^{19}\,{\rm cm^{-2}}$) and appears clumpy with finger-like projections. At negative velocities closer to zero (Figure 2, top right), the H I emission is more extended and contains a filament that appears similar to F2 ($N_{\rm HI} \sim 2 \times 10^{20}\,{\rm cm^{-2}}$) and breaks off into another V-shape structure (F2V, $N_{\rm HI} \sim 1.7 \times 10^{20}\,{\rm cm^{-2}}$). At positive velocities closer to zero (Figure 2, bottom left), the H I emission exhibits the F1K morphology ($N_{\rm HI} \sim (3.8\text{–}5.4) \times 10^{20}\,{\rm cm^{-2}}$) and contains emission along the edge of F1V ($N_{\rm HI} \sim 2.3 \times 10^{20}\,{\rm cm^{-2}}$). At higher positive velocities (Figure 2, bottom right), the H I gas is primarily located in the southwest corner ($N_{\rm HI} \sim 4.5 \times 10^{19}\,{\rm cm^{-2}}$ to $1 \times 10^{20}\,{\rm cm^{-2}}$) and does not resemble any structures associated with the local gas. The H I emission at $|v_{\rm lsr}| \gtrsim 20\ {\rm km\ s^{-1}}$ (Figure 2, top left and bottom right) contains nonlocal gas with velocities consistent with intermediate-velocity clouds (IVCs).

3.3. Comparison of Radio Polarization Gradient and H I Structures

We compared structures in the polarization gradient to H I emission. Figure 3 shows the 1.4 GHz GALFACTS polarization gradient (red) with GALFA-H I velocity channel maps (blue) overlaid at a $v_{\rm lsr}$ of $-5.5\ {\rm km\ s^{-1}}$ (left), $+0.4\ {\rm km\ s^{-1}}$ (middle), and $+7.0\ {\rm km\ s^{-1}}$ (right). These multiphase tracers clearly share a common orientation and similar morphologies in this region, although they are not always spatially coincident. The observed alignment is quantified later in Section 4.4.

The H I emission shows similar morphological structures and orientations to the polarization gradient across a range of velocities. At $v_{\rm lsr} \sim -5.5\ {\rm km\ s^{-1}}$ (Figure 3, left), there is a prominent filamentary structure that is aligned with F2S. In light of this alignment, we consider this H I filament to be morphologically associated with F2. At $v_{\rm lsr} \sim +0.4\ {\rm km\ s^{-1}}$ (Figure 3, middle), only the F2S portion is seen in H I and extends farther south, highlighting F2V. At $v_{\rm lsr} \sim +7\ {\rm km\ s^{-1}}$ (Figure 3, right), the H I emission is more extended and "fills in" F1K.

3.4. Hα Emission

G216 is covered by VTSS in the composite Hα map (Finkbeiner 2003) and contains a prominent Hα filament ($I_{\rm H\alpha} \sim 3\text{–}7$ R, where $1\ {\rm R} \equiv 10^6/4\pi$ photons cm^{-2} s^{-1} sr^{-1}) shown in Figure 4 (left). The VTSS Hα filament clearly contains the F1K ($I_{\rm H\alpha} \sim 3\text{–}5$ R) and F1V ($I_{\rm H\alpha} \sim 3\text{–}7$ R) morphologies. This filament runs along the edge of extended emission ($I_{\rm H\alpha} \sim 3$ R) that is primarily located in the northeast corner with an intensity that is roughly twice as high as that of the southwest corner, where there

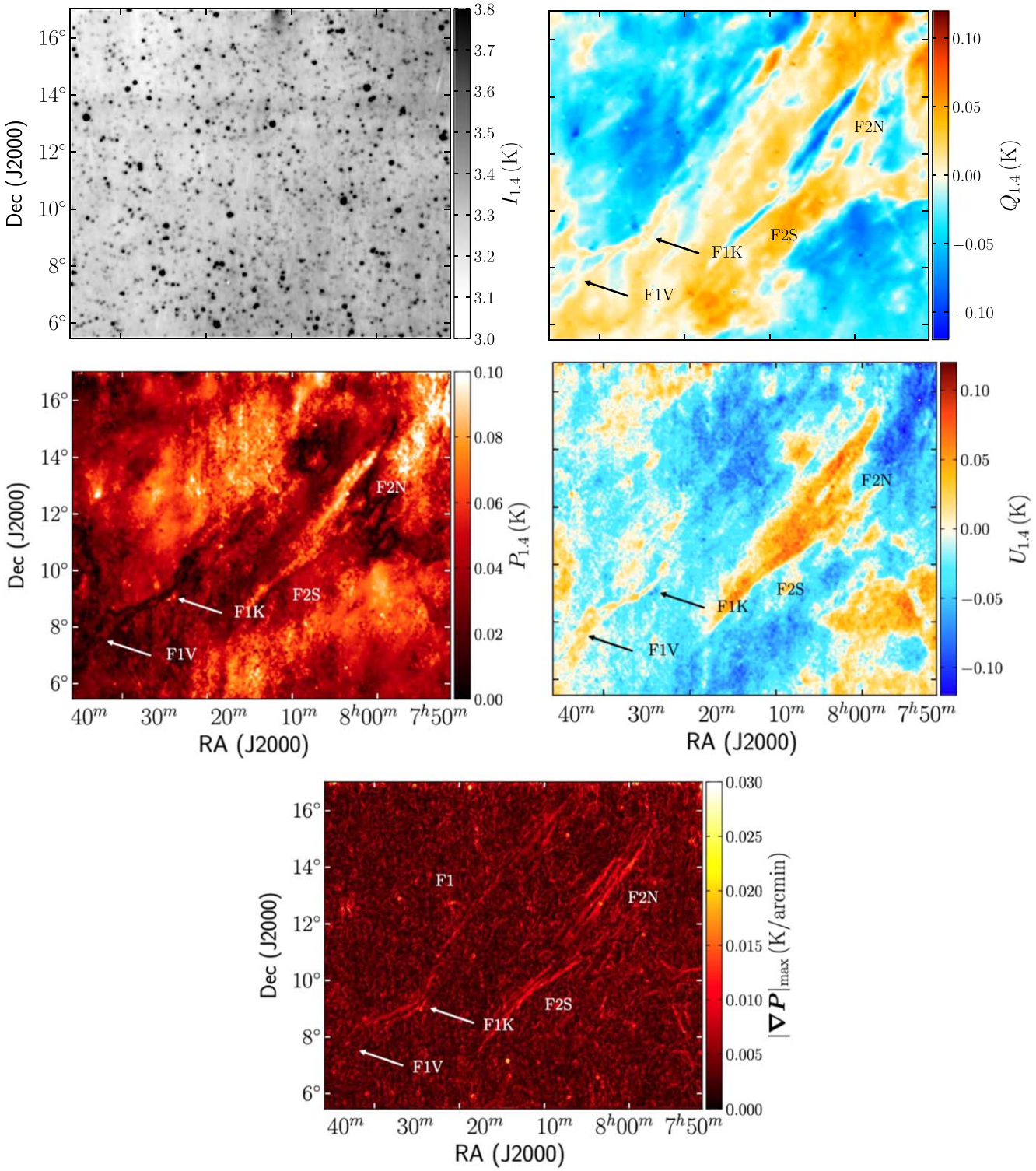

Figure 1. 1.4 GHz GALFACTS data of G216 at 5′ angular resolution. Shown are $I_{1.4}$ (top left), $P_{1.4}$ (middle left), $Q_{1.4}$ (top right), $U_{1.4}$ (middle right), and $|\nabla \boldsymbol{P}|_{\max}$(bottom center). The polarization data have been destriped, and bright polarized sources have been removed. The locations of F1 and F2 as discussed in the text are indicated.

is little emission. There is also a suggestion of linear features in the extended Hα emission in the northeast corner with roughly the same orientation as F1.

Figure 4 (middle) shows the WHAM Hα emission at a velocity of $v_{\rm lsr} = +7.3\,{\rm km\,s^{-1}}$, corresponding to the approximate peak velocity of the emission toward F1. The small-scale Hα filament seen in the VTSS data corresponds to a larger, more extended filament in the WHAM data ($I_{\rm H\alpha} \sim 4$ R). Similar to the VTSS results, the WHAM filament lies along the edge of lower-intensity diffuse emission ($I_{\rm H\alpha} \sim 3$ R) in the northeast corner that is roughly twice as high as that of the southwest.

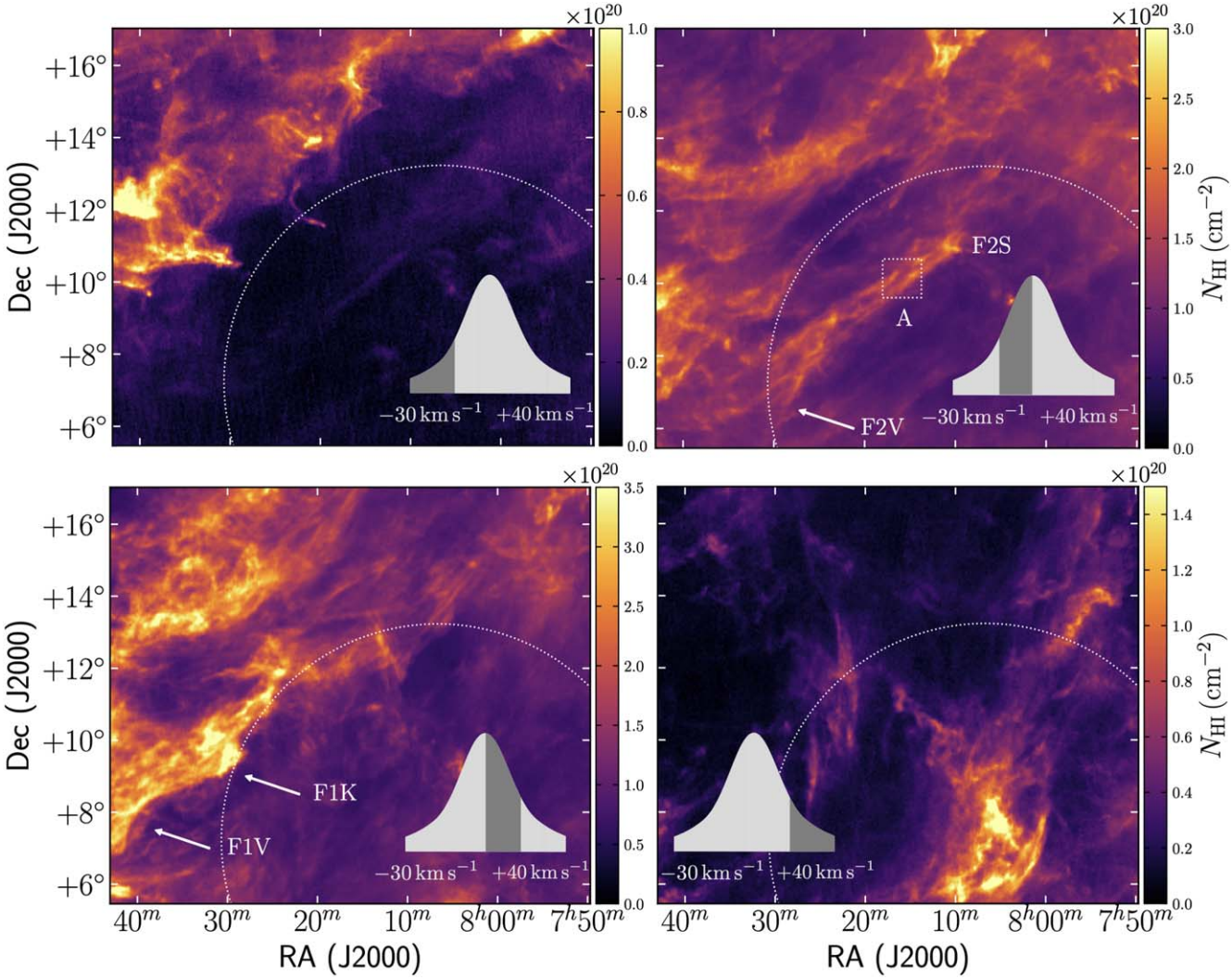

Figure 2. GALFA-H I column density maps of G216 at 3.′5 resolution across the full velocity range. The data were integrated over $-30\ \mathrm{km\ s^{-1}} \leqslant v_{\rm lsr} \leqslant -10\ \mathrm{km\ s^{-1}}$ (top left), $-10\ \mathrm{km\ s^{-1}} \leqslant v_{\rm lsr} \leqslant +4\ \mathrm{km\ s^{-1}}$ (top right), $+4\ \mathrm{km\ s^{-1}} \leqslant v_{\rm lsr} \leqslant +20\ \mathrm{km\ s^{-1}}$ (bottom left), and $+20\ \mathrm{km\ s^{-1}} \leqslant v_{\rm lsr} \leqslant +40\ \mathrm{km\ s^{-1}}$ (bottom right) to show various features in the data. Locations of F1 and F2 as discussed in the text are indicated. Note the different intensity scales between panels. The lower corner of each panel indicates the range in $v_{\rm lsr}$. The segmented dotted circles (white) show the approximate location of the projected low column density region discussed in Section 3.6. Region A marked by the dotted rectangle (white) in the top right panel indicates the subset of the field for which we apply the ROHSA phase separation in Section 4.3.

The VTSS filament is spatially coincident with F1 and lies between the double-jump morphology of F1K. Figure 4 (right) shows the correspondence between the polarization gradient (red) and VTSS Hα emission (green).

3.5. Thermal Dust Emission

Figure 5 (left) shows the Planck I_{353} dust thermal emission. The dust emission is strongly correlated with the local H I gas found at velocities $-10\ \mathrm{km\ s^{-1}} \lesssim v_{\rm lsr} \lesssim +20\ \mathrm{km\ s^{-1}}$, showing the same F1K ($I_{353} \sim 0.4\ \mathrm{MJy\ sr^{-1}}$), F2S ($I_{353} \sim 0.2\ \mathrm{MJy\ sr^{-1}}$), and F2V ($I_{353} \sim 0.3\ \mathrm{MJy\ sr^{-1}}$) morphologies. Along F1K and F1V, the VTSS filament is slightly displaced from the edge of the dust emission toward the direction of the Galactic plane. Figure 5 (right) shows the VTSS Hα emission (green) with the Planck I_{353} dust emission (magenta) overlaid to highlight this spatial separation between the ionized and neutral medium along F1.

3.6. The Surrounding Area

The G216 filaments lie along the northern edge (in Galactic coordinates) of a low column density region seen in the projected VTSS Hα ($I_{\rm H\alpha} \sim 1.2$ R), H I ($N_{\rm H\,I} \sim 3 \times 10^{20}\ \mathrm{cm^{-2}}$), and Planck dust ($I_{353} \sim 0.2\ \mathrm{MJy\ sr^{-1}}$) emission just above the Galactic plane. Figure 6 shows a $\sim 50^\circ \times 50^\circ$ region of the surrounding area in VTSS Hα emission (green) and Planck I_{353} dust emission (magenta) in Galactic coordinates. The G216 footprint investigated in this paper is indicated with a rectangle (white), and the approximate location of the projected low column density region is shown with a $\sim 10^\circ$-diameter dotted circle (white) centered on $(\ell, b) \sim (215^\circ, +20^\circ)$. The location of F1 is indicated and is clearly oriented roughly parallel to the Galactic plane. The cavity is roughly circular in dust emission and triangular in Hα emission. The Hα emission that is morphologically associated with our field extends as far west as $\ell \sim 195^\circ$, but this is beyond the VTSS footprint in a region where the GALFACTS are yet to be processed. We do not

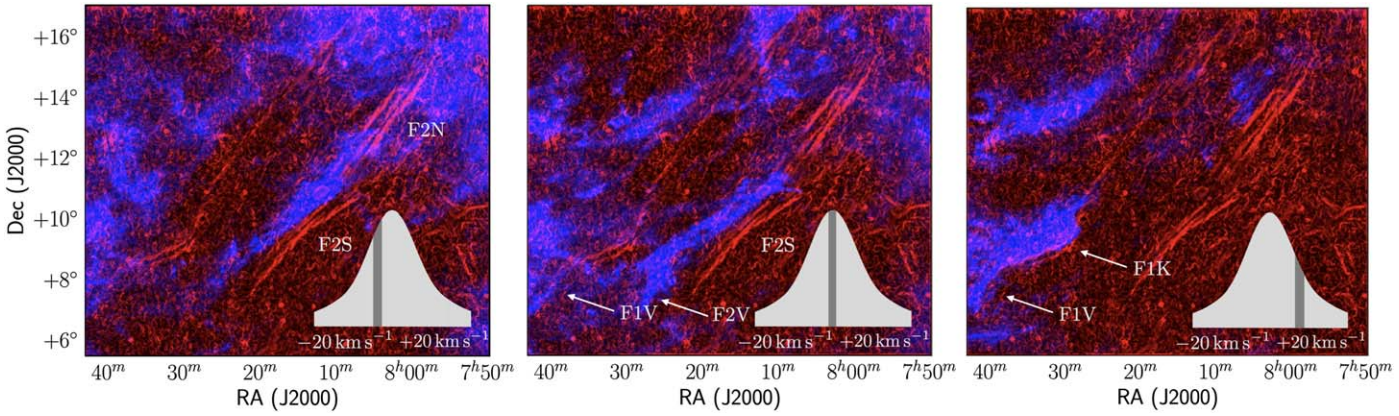

Figure 3. Destriped GALFACTS $|\nabla P|_{\max}$ of G216 at 5′ resolution (red) with GALFA-H I velocity channel maps (blue) at a $v_{\rm lsr}$ of −5.5 km s^{-1} (left), + 0.4 km s^{-1} (middle), and + 7.0 km s^{-1} (right) overlaid. $|\nabla P|_{\max}$ is on a linear scale spanning 0–0.01 K arcmin^{-1}, and the H I channel maps are on a linear scale over 2–4 K (left), 4–9 K (middle), and 5–18 K (right). Locations of F1 and F2 associated with H I emission as discussed in the text are indicated.

extend our footprint farther east, as the current footprint contains the full extent of the polarization gradient filaments in this region.

There are two nearby Hα filaments that were located using WHAM data (Haffner et al. 1998; see their Figure 1 that includes our footprint). There is a vertical (in Galactic coordinates) Hα filament located at $\ell \sim 225°$ centered on $v_{\rm lsr} = +20$ km s^{-1} with a curved filament found at its northern end where the peak emission extends from $\ell \sim 220°$ centered on $v_{\rm lsr} = -20$ km s^{-1} to $\ell \sim 235°$ centered on $v_{\rm lsr} = +20$ km s^{-1}. The magnitudes of these velocities are higher than the peak velocity of $v_{\rm lsr} = 7.3$ km s^{-1} that we find for the F1-associated Hα emission. We do not find polarization gradient structures associated with these Hα filaments using the 5′ GALFACTS data. The F1K structure of our field, as well as the nearby Hα filaments (Haffner et al. 1998), can also be seen in Figure 2 of Finkbeiner (2003).

4. Analysis

4.1. Synchrotron Polarization

We computed the POS synchrotron pseudo−magnetic field orientation via $\theta_{1.4} = (1/2)\arctan(U_{1.4}/Q_{1.4})$. We first multiplied $Q_{1.4}$ and $U_{1.4}$ by −1, corresponding to a 90° rotation in the polarization angle since the magnetic field orientation is orthogonal to that of the electric field. Derotating the synchrotron polarization angles can in principle remove Faraday rotation effects and provide the intrinsic magnetic field direction. However, the structures in this paper are not spatially correlated with excess synchrotron emission, so derotation would yield the magnetic field orientation of the background synchrotron-emitting source rather than the foreground Faraday-rotating structures of interest. As a measure of the combined magnetic field orientation and Faraday rotation, $\theta_{1.4}$ remains a valuable quantity.

Figure 7 shows the 5′ polarization gradient map with $\theta_{1.4}$ overlaid as pseudovectors (white, to distinguish this from the true magnetic field direction) with lengths that are proportional to $P_{1.4}$. The orientation of $\theta_{1.4}$ is noticeably coherent in many areas of the field, particularly in the northeast and southwest corners, as well as along the length of F2. There are drastic changes in $\theta_{1.4}$ along F1K and F1V, as well as along the edges of F2, where the pseudo−magnetic field orientation suddenly becomes oriented parallel to the filaments.

4.2. Dust Polarization

We computed the POS magnetic field orientation of the dust emission using the 80′ Planck Q_{353} and U_{353} maps via $\theta_{353} = (1/2)\arctan(U_{353}/Q_{353})$. The Stokes maps were both first multiplied by −1, corresponding to a 90° rotation in the polarization angle. Figure 5 (left) shows θ_{353} overlaid on I_{353} as textured lines using LICPY (Cabral & Leedom 1993).[15] The magnetic field direction is generally parallel to F1 and F2, except where it follows the morphology of F2V and changes direction around an R.A. of $\sim 8^{\rm h}$.

4.3. Magnetically Aligned, Cold H I Structures

The identification of magnetically aligned H I structures was made using the Rolling Hough Transform (RHT),[16] a machine vision algorithm that identifies and parameterizes coherent, linear structures in an image (Clark et al. 2014). The RHT provides an array of linear intensities binned by an angle θ measured from the vertical for each pixel, $R(\theta, x, y)$, quantifying the probability that each pixel is associated with a coherent linear structure. The RHT backprojection visualizes the resulting linear features by integrating $R(\theta, x, y)$ over θ. The RHT uses three input parameters: a smoothing kernel diameter D_K, a window diameter D_W, and a linear intensity threshold Z. Details on the RHT procedure are further described by Clark et al. (2014).

We applied the RHT to the GALFA-H I data over the velocity range -20 km s$^{-1} \lesssim v_{\rm lsr} \lesssim +20$ km s^{-1}, integrating over four spectral channels corresponding to a ~ 3 km s^{-1} velocity binning. Based on the results of Clark et al. (2014), we use the RHT parameters $D_W = 100'$, $D_K = 10'$, and $Z = 70\%$. The H I RHT backprojections are shown in Figure A.1.

To investigate the thermal properties of narrow H I structures, we used the Regularized Optimization for Hyper-Spectral Analysis (ROHSA) Gaussian decomposition code (Marchal et al. 2019).[17] The complexity of the H I line varies considerably over this region, as does the number of Gaussians required to describe them. This is particularly true along LOSs that contain IVCs. As a result, the fixed number of Gaussians in ROHSA presents a considerable challenge for G216: increasing

[15] https://rufat.be/licpy/
[16] https://github.com/seclark/RHT
[17] https://github.com/antoinemarchal/ROHSA

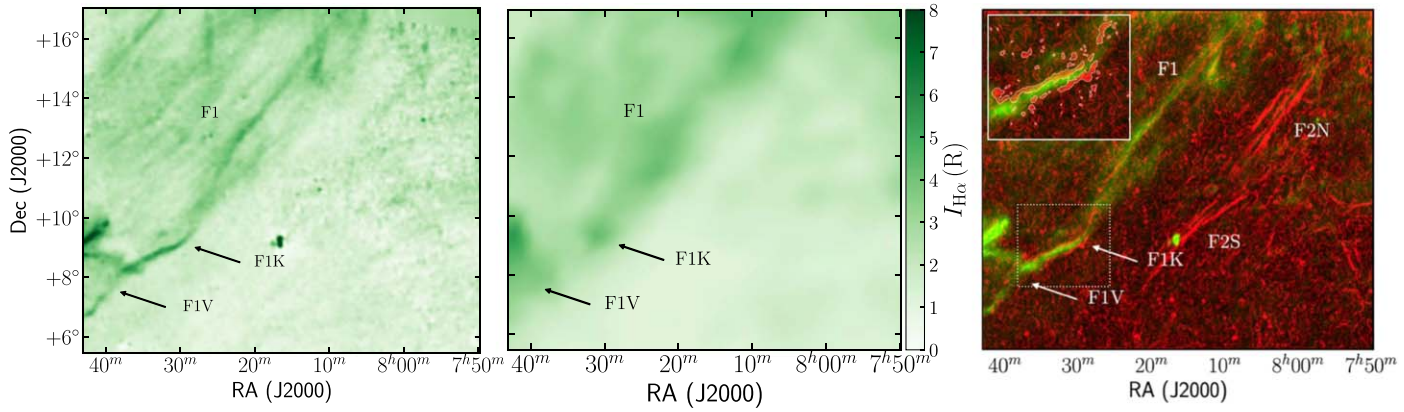

Figure 4. Left: VTSS Hα emission of G216. Middle: WHAM Hα emission at $v_{\rm lsr} = +7.3$ km s^{-1}, the approximate peak Hα velocity of F1. Right: $|\nabla \boldsymbol{P}|_{\rm max}$(red) with VTSS H$\alpha$ emission (green) overlaid. The figure inset shows the F1K region with a 0.006 K arcmin^{-1} level contour of $|\nabla \boldsymbol{P}|_{\rm max}$(white) overlaid. The $|\nabla \boldsymbol{P}|_{\rm max}$ intensity is on a linear scale from 0 to 0.01 K arcmin^{-1}, and the Hα intensity is on a squared intensity from 0 to 6 R. The locations of F1 and F2 as discussed in the text are indicated.

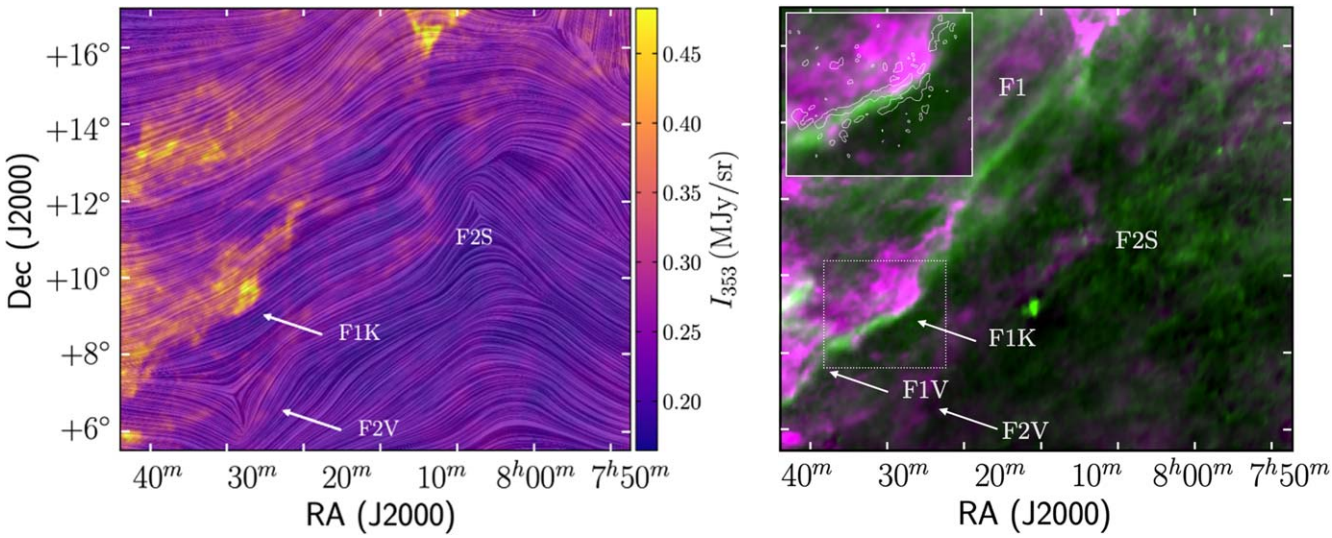

Figure 5. Planck I_{353} thermal dust emission (magenta) of G216. Left: the POS magnetic field orientations derived using Q_{353} and U_{353} are overlaid as textured lines. Locations of F1 and F2 associated with dust emission as discussed in the text are indicated. Right: VTSS Hα emission (green) is shown to highlight the spatial separation of the ionized and neutral media along F1. The figure inset shows the F1K region with a 0.006 K arcmin^{-1} level contour of $|\nabla \boldsymbol{P}|_{\rm max}$(white) overlaid. The H$\alpha$ intensity is on a linear scale spanning 0.5–7 R, and the I_{353} intensity is on a linear scale over 0.2–0.4 MJy sr^{-1}.

the number of Gaussians to accurately fit the IVCs causes other regions to become overfit, affecting the overall phase separation. Overcoming this requires subdividing the region into several smaller subregions and creating a mosaic of the resulting phase-separated components. This is beyond the scope of this work, so we focus on a single subregion toward F2 (region A) indicated with a dotted rectangle (white) in the top right panel of Figure 2.

ROHSA is based on a regularized nonlinear least-squares criterion that accounts for the spatial coherence of H I emission by applying a Laplacian filtering to the parameter maps that penalize small spatial frequencies and for the multiphase nature of the atomic medium by minimizing the variance in velocity dispersion. We set the maximum number of Gaussians fit with ROHSA along each LOS to five, and we set the four hyperparameters that control the strength of the regularization equal to 10 (see Marchal et al. 2019 for details). The magnitude of the hyperparameters was empirically chosen to converge toward a noise-dominated residual that is roughly constant across the field (with an average reduced chi-square of $\sim$1.4) while minimizing the number of Gaussians used. A decomposition using six Gaussians does not qualitatively change our results for the local gas.

The local H I emission with $|v_{\rm lsr}| \lesssim 10$ km s^{-1} was well represented using three Gaussian components, G_1, G_2, and G_3, with mean velocity dispersions weighted by column density, respectively, of $\langle \sigma_1 \rangle = 1.4$ km s^{-1}, $\langle \sigma_2 \rangle = 4.0$ km s^{-1}, and $\langle \sigma_3 \rangle = 8.4$ km s^{-1}, reminiscent of the three-phase neutral ISM composed of CNM, UNM, and WNM. These Doppler line widths are a mixture of thermal and turbulent contributions and lead to upper-limit kinetic temperatures of $T_{K,1} \sim 250$ K, $T_{K,2} \sim 1990$ K, and $T_{K,3} \sim 8600$ K, respectively. Gaussians G_4 and G_5 were used to encode intermediate-velocity gas with a velocity centroid $v_{\rm lsr} \gtrsim 10$ km s^{-1}.

Figure 8 (left) shows the H I brightness temperature map at $v_{\rm lsr} = -1.8$ km s^{-1} corresponding to the peak of the average spectrum in region A. The contours (white) show the RHT backprojection applied to the H I channel map with a velocity channel width of 0.8 km s^{-1} using the same parameters as those used on the binned velocity channels. The column density map

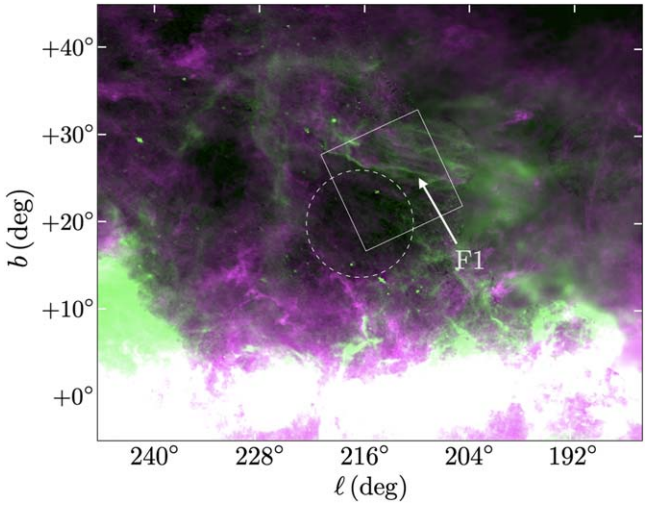

Figure 6. VTSS Hα (green) and Planck I_{353} dust (magenta) emission for a larger ∼50° × 50° field of the surrounding area in Galactic coordinates. The footprint of the region presented in this paper and the low column density region are indicated by the rectangle (white) and dotted circle (white), respectively. The location of F1 is also indicated. The Hα intensity is on a linear scale over 0.1–10 R, and the I_{353} dust intensity is on a square root scale spanning 0.2–1.5 MJy sr^{-1}.

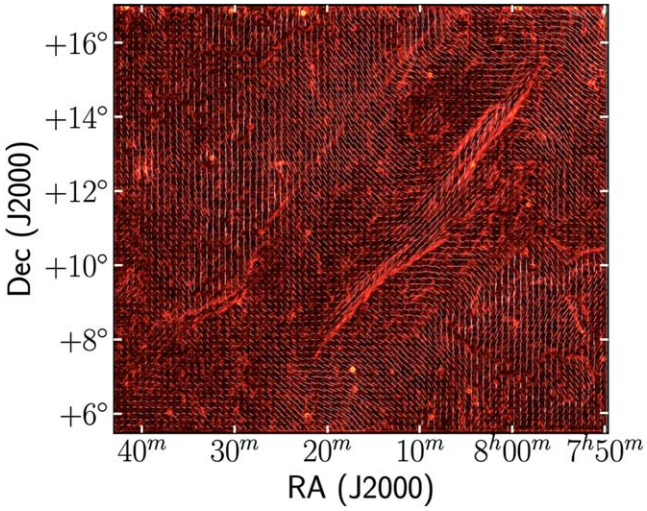

Figure 7. Destriped GALFACTS $|\nabla \boldsymbol{P}|_{\rm max}$ of G216 at 5′ resolution, with the polarization angles derived from $Q_{1.4}$ and $U_{1.4}$ rotated by 90° shown as line segments with lengths that are weighted by $P_{1.4}$. The $|\nabla \boldsymbol{P}|_{\rm max}$ intensity scale is the same as that shown in Figure 1 (bottom right).

of the local CNM component, of particular interest for our RHT analysis, is shown in Figure 8 (right) under the optically thin assumption of Equation (2). The small-scale filamentary structures identified with the RHT in the peak channel map are strongly correlated with the CNM component.

We inspected the spectral decomposition toward three LOSs. Figure 9 shows the spectral decomposition for LOSs a, b, and c indicated with circles (black) in Figure 8, where a and c are toward filamentary H I structures and b is toward more extended emission between them. The LOSs toward narrow H I structures clearly have significant CNM components, while that of more extended H I emission is UNM and WNM dominated. Toward this portion of F2, linear H I structures are dominated by CNM over a velocity range of −10 km s^{-1} $\lesssim v_{\rm lsr} \lesssim$ 0 km s^{-1}, suggesting that narrow H I structures outside of this range are likely WNM dominated. A more complete ROHSA analysis is required to determine whether this applies to the entire G216 field.

4.4. Comparison of Polarization Gradient Filament and Narrow H I Structure Orientation

Structures in radio polarization gradients primarily trace properties of the magnetized warm ionized gas (e.g., Haverkorn et al. 2004a, 2004b; Hill et al. 2008; Gaensler et al. 2011), while narrow H I structures tend to be associated with cold neutral gas (Clark et al. 2019; Peek & Clark 2019; Kalberla & Haud 2020) that is coupled to the ambient magnetic field (Clark et al. 2014, 2015; Martin et al. 2015; Kalberla et al. 2016; Blagrave et al. 2017). To investigate whether these very different environments of the ISM share a common magnetic field, we compare the orientation of polarization gradient filaments to that of narrow H I structures.

Our visual inspection showed that structures in the GALFACTS polarization gradient and GALFA-H I emission share similar morphologies and a common orientation (Section 3.3). To perform a more quantitative comparison, we compared the distributions of RHT orientations between $|\nabla \boldsymbol{P}|_{\rm max}$, H I, and Hα. We applied the RHT to maps of the destriped 5′ polarization gradient and Hα emission using the same input parameters as applied to the binned H I channel maps (Section 4.3). The RHT backprojections of $|\nabla \boldsymbol{P}|_{\rm max}$ and Hα emission are shown in Figures A.2 and A.3, respectively.

Figure 10 shows the RHT orientation distributions of $|\nabla \boldsymbol{P}|_{\rm max}$(red), Hα (green), and H I (blue) across an H I velocity range −20 km s^{-1} $\lesssim v_{\rm lsr} \lesssim$ +20 km s^{-1}. An angle of 0° is vertical in the image plane and increases anticlockwise (Clark et al. 2014). The polarization gradient filaments are very well aligned with structures in Hα emission, although the latter has a slightly wider distribution. In general, the peak H I orientation tends to be ∼10° clockwise from the polarization gradient filaments. At velocities −20 km s^{-1} $\lesssim v_{\rm lsr} \lesssim$ +5 km s^{-1}, the H I emission is mostly single peaked and strongly aligned with the polarization gradient filaments. The H I emission becomes somewhat double peaked at +6 km s^{-1} $\lesssim v_{\rm lsr} \lesssim$ +11 km s^{-1}, while the more dominant H I orientation remains strongly aligned with the polarization gradient filaments. At $v_{\rm lsr} \gtrsim$ +15 km s^{-1}, the H I orientation is less organized. These RHT results demonstrate that the filamentary structures in the polarization gradient are, in general, well aligned with the small-scale Hα and H I structures across a wide H I velocity range.

4.5. GALFACTS Depolarization

We find several notable depolarized regions in the GALFACTS data. There is a ∼2°-wide depolarized band between F1 and F2 that is spatially correlated with extended WHAM Hα emission. Figure 11 shows the GALFACTS polarized intensity with WHAM Hα intensity contours at $v_{\rm lsr}$ = +7.3 km s^{-1} overlaid (white). This velocity channel roughly corresponds to the peak Hα velocity of F1. There are also two thin filamentary features along F1K with sizes comparable to the angular resolution where the GALFACTS polarized intensity drops to zero that are consistent with "depolarization canals": narrow, elongated structures in depolarization caused by strong gradients in the RM (Haverkorn & Heitsch 2004). The double-jump polarization gradient feature along F1K highlights the edges of the associated RM

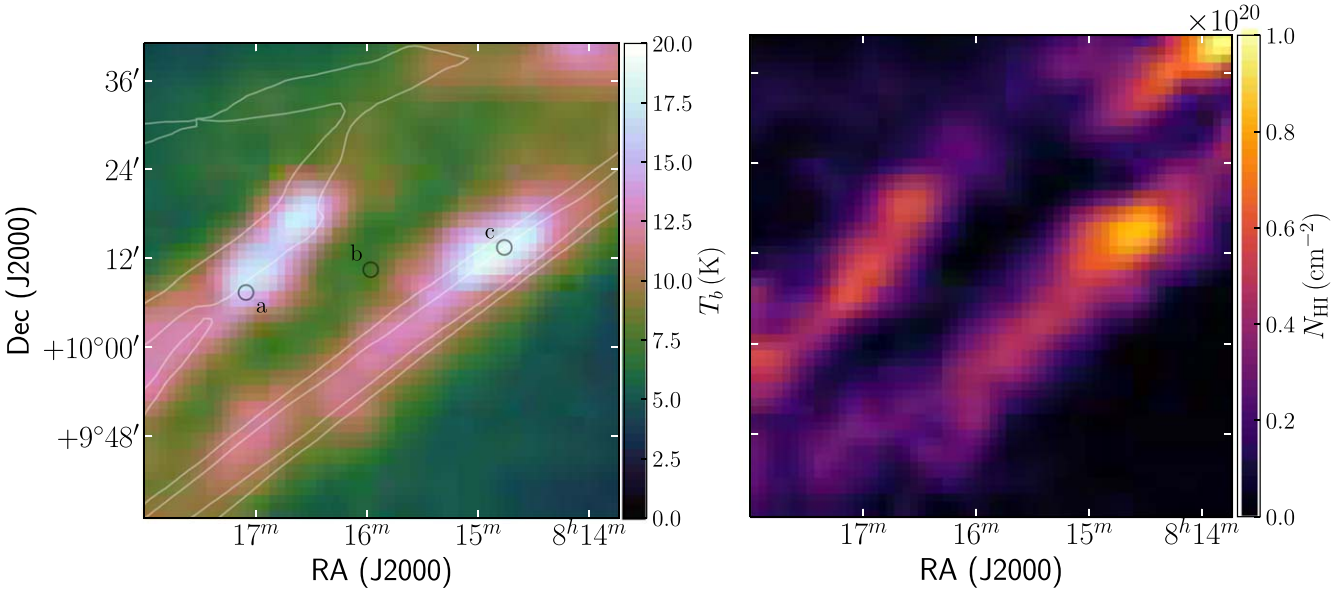

Figure 8. Small subset of the GALFA-H I data toward F2, designated region A, as indicated with the dotted rectangle (white) in the top right panel of Figure 2. Left: velocity channel map at the peak of the mean spectrum corresponding to $v_{\rm lsr} = -1.8$ km s^{-1}. The RHT backprojection is overlaid as contours (white) using levels of 0.1 and 0.5. The circles (black) mark the LOSs toward which we show the phase-separated spectra in Figure 9. Right: column density map of the local CNM emission (G_1) derived with ROHSA.

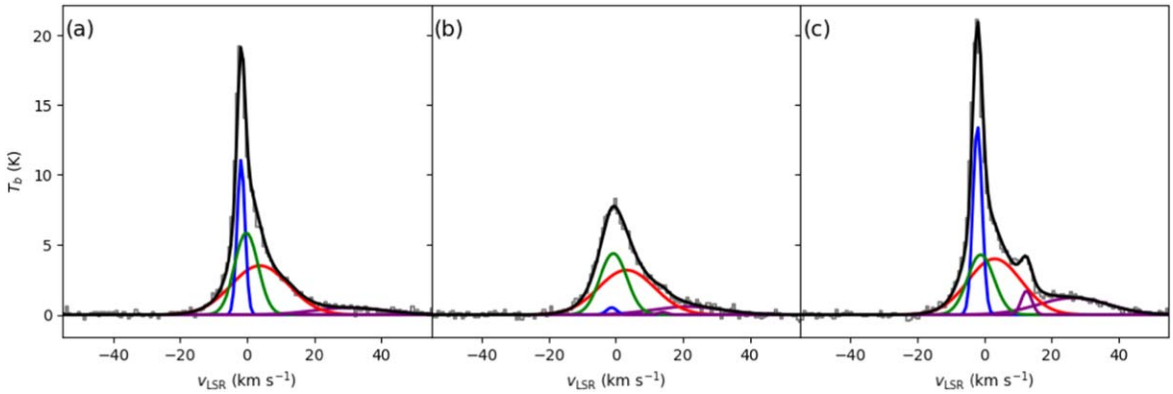

Figure 9. ROHSA Gaussian decomposition for the three LOSs toward region A indicated in Figure 8 (left). The GALFA-H I data are shown in gray, while the total emission described by ROHSA is shown in black. The CNM, UNM, and WNM components of the local gas are shown in blue, green, and red, respectively. The two components used to describe the IVC are shown in purple.

structure and reflects the strong spatial gradient in degree of Faraday rotation.

4.6. 3D RM Synthesis

To investigate the Faraday-rotating magnetoionic medium, we applied RM synthesis (Brentjens & de Bruyn 2005) to the GALFACTS polarization data. For a single rotating medium that is not emitting any polarized emission, the RM of a polarized source can be measured by the line of best fit to the observed χ versus the square of the observing wavelength λ^2,

$$\left(\frac{\chi}{\rm rad}\right) = \left(\frac{\chi_0}{\rm rad}\right) + \left(\frac{\rm RM}{\rm rad\ m^{-2}}\right)\left(\frac{\lambda}{\rm m}\right)^2, \quad (3)$$

where χ_0 is the incident polarization angle. However, the relationship shown in Equation (3) does not generally hold for Galactic synchrotron emission, where there are often multiple rotating foregrounds, as well as a mixture between synchrotron-emitting and Faraday-rotating gas (Ferrière 2016). The development of RM synthesis (Burn 1966; Brentjens & de Bruyn 2005) allows diffuse polarized emission to be described as a function of Faraday rotation characterized by the Faraday depth ϕ. The Faraday depth is related to n_e and $B_\parallel$ via

$$\left(\frac{\phi(L)}{\rm rad\ m^{-2}}\right) = 0.81 \int_L^0 \left(\frac{n_e}{\rm cm^{-3}}\right)\left(\frac{B_\parallel}{\mu\rm G}\right)\left(\frac{d\ell}{\rm pc}\right), \quad (4)$$

where L is the distance to the polarized emission and $d\ell$ is the infinitesimal path length along the LOS. The integral is taken from the source of the polarized emission to the observer, setting the convention that a positive (negative) ϕ indicates an LOS magnetic field direction that is pointing toward (away from) the observer (see Ferrière et al. 2021 for details on Faraday rotation conventions).

Many key quantities in RM synthesis are dependent on the frequency coverage of the polarization data. The Faraday depth resolution is the FWHM of the primary lobe in the RM structure function (RMSF) determined by the λ^2 coverage via $\delta\phi \approx 3.8/\Delta(\lambda^2)$, where $\Delta(\lambda^2) = \lambda^2_{\rm max} - \lambda^2_{\rm min}$. We have used

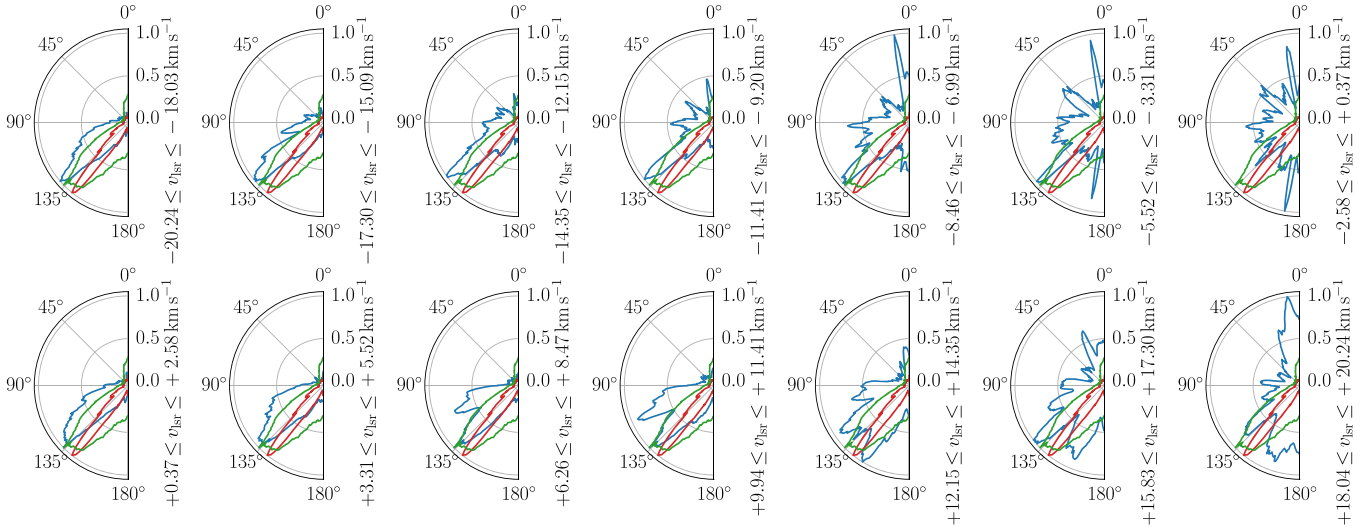

Figure 10. RHT orientations of the destriped 5′ $|\nabla \boldsymbol{P}|_{\max}$ (red), Hα emission (green), and velocity channel H I fibers (blue). The distributions of $|\nabla \boldsymbol{P}|_{\max}$ and Hα are the same in each panel, while those of H I are a function of binned H I velocity. All histograms have been normalized to the same intensity scale and rotated such that an orientation of 0° is vertical in the image plane.

3.8 in replacement of $2\sqrt{3}$ from Equation (61) of Brentjens & de Bruyn (2005) as a more accurate measure of the FWHM of a sinc function (e.g., Schnitzeler et al. 2009). The maximum detectable Faraday depth corresponds to a ∼50% drop in sensitivity across a single frequency channel given by $\phi_{\max} \approx 1.9/\delta(\lambda^2)$ and quantifies the gradual loss in sensitivity at large Faraday depths. Lastly, the maximum Faraday depth scale is the broadest detectable Faraday depth feature given by $\phi_{\max-\mathrm{scale}} \approx \pi/\lambda^2_{\min}$, where Faraday structures broader than this will be significantly depolarized.

We applied 3D RM synthesis to the GALFACTS frequency cubes using the `RMtools` package developed by the Canadian Initiative for Radio Astronomy Data Analysis (CIRADA; Purcell et al. 2020).[18] This software inputs Stokes Q and U frequency cubes and returns a Faraday depth cube containing a ϕ spectrum at every spatial pixel. Prior to performing RM synthesis, we flagged 15 frequency channels (4%) that showed strong RFI. Flagging RFI channels does not significantly affect the Faraday depth resolution or the maximum detectable Faraday depth. The frequency channel maps were also destriped and smoothed to 5′ angular resolution following the procedure outlined in Section 3.1.

We computed the ϕ spectra over a Faraday depth range of $\pm 4000\,\mathrm{rad\,m^{-2}}$ to include a large baseline for uncertainty measurements, and we used a sampling of 5 points across the RMSF FWHM for Gaussian fitting. The GALFACTS weights are nearly equal as a function of frequency for any given spatial pixel (Leahy 2018), so we applied a uniform weight to the unflagged channels. The GALFACTS frequency coverage results in a Faraday depth resolution of $\delta\phi = 403\,\mathrm{rad\,m^{-2}}$, maximum Faraday depth $\phi_{\max} \approx 7 \times 10^4\,\mathrm{rad\,m^{-2}}$, and maximum Faraday depth scale of $\phi_{\max-\mathrm{scale}} = 81\,\mathrm{rad\,m^{-2}}$.

We used `RM-clean` (Heald et al. 2009) to fit a Gaussian to the primary lobe of the RMSF to deconvolve the Faraday depth spectra. We find an RMSF FWHM of $396\,\mathrm{rad\,m^{-2}}$ with a standard deviation of $2 \times 10^{-4}\,\mathrm{rad\,m^{-2}}$ measured across the field. This is only ∼1% narrower than the expected theoretical value. We cleaned the Faraday depth spectra down to a threshold of 10 times the noise level in the spectra to prevent false identification of clean components. Cleaning the Faraday depth spectra has no significant effect on our results, nor does increasing the cleaning threshold.

We applied a Gaussian fitting procedure to each of the cleaned Faraday depth spectra. The spectral baseline was used to estimate the uncertainty in the polarized intensity over the Faraday depth range $|\phi| \geqslant 2000\,\mathrm{rad\,m^{-2}}$ far from the polarized signal. We estimated the rms uncertainty for each of the Q and U components as σ_Q and σ_U, respectively, along the spectral baseline, and we compute the corresponding uncertainty in the polarized intensity via $(1/\sigma_P)^2 = (1/\sigma_Q)^2 + (1/\sigma_U)^2$. The S/N of the brightest peak in Faraday depth, $P_{\mathrm{S/N}}$, was determined as the ratio of the peak polarized intensity derived from the Gaussian fit to the baseline uncertainty in polarized intensity. The peak Faraday depth ϕ_{peak} corresponds to the Faraday depth at the peak polarized intensity with an estimated uncertainty of

$$\sigma_{\phi_{\mathrm{peak}}} = \frac{\mathrm{RMSF\ FWHM}}{2\,P_{\mathrm{S/N}}}, \tag{5}$$

where we use the RMSF FWHM from `RM-clean`. Based on the results of George et al. (2012), we applied a detection threshold of $P_{\mathrm{S/N}} \geqslant 10$ to minimize false detections.

Our Gaussian fitting results of the cleaned Faraday depth spectra are summarized in Figure 12. This includes the peak Faraday depth ϕ_{peak} (top), uncertainty in the peak Faraday depth $\sigma_{\phi_{\mathrm{peak}}}$ (middle), and S/N in the peak polarized intensity $P_{\mathrm{S/N}}$ (bottom). The uncertainty in polarized intensity is roughly uniform over the field with a mean value of $\langle\sigma_P\rangle = (6 \pm 1) \times 10^{-4}\,\mathrm{K}$. There is increased Faraday rotation toward both F1K and F1V. The sign of ϕ_{peak} is generally positive, indicating an LOS magnetic field direction that is mostly pointing toward the observer.

5. Physical Properties of F1

To quantify our comparison of the magnetized ionized and neutral media of this region, we determine several key astrophysical quantities. As F1K is a well-defined structure

[18] https://github.com/CIRADA-Tools/RM-Tools

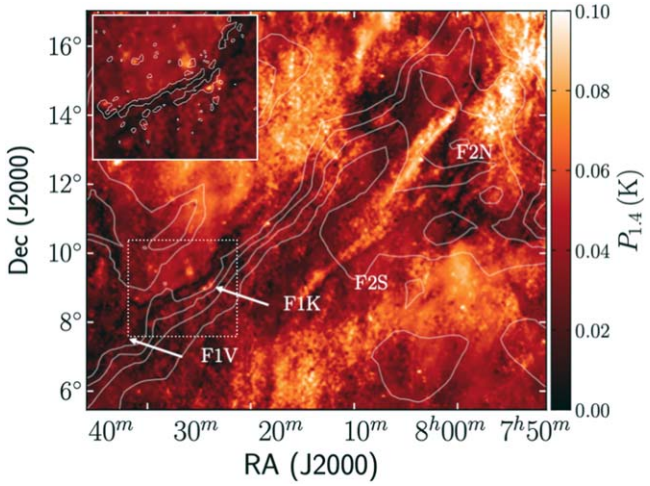

Figure 11. Destriped GALFACTS polarized intensity of G216 at 5′ resolution. The WHAM Hα contours overlaid (white) are for $v_{\rm lsr} = +7.3$ km s^{-1}, roughly corresponding to the peak velocity of F1K, and include levels of 1.6, 2.0, 2.4, and 2.8 R. The figure inset shows the F1K region with a 0.006 K arcmin^{-1} level contour of $|\nabla \boldsymbol{P}|_{\rm max}$(white) overlaid. The locations of F1 and F2 as discussed in the text are indicated.

with significant detections in all of our multiphase tracers, our quantitative analysis focuses on this portion of F1. This structure is most prominent in Hα emission, so we defined an "on" region by the curved F1K portion of the filament in Hα emission, while the "off" region was taken to be an adjacent curved region of the same size to the immediate west of this portion of the filament. To reduce potential bias from outliers, we measure the "on" and "off" signals as the median value of the "on" and "off" regions, respectively. Unless stated otherwise, all final measurements in this section are made via subtracting the "off" from the "on" region to minimize foreground and/or background contributions.

5.1. Distance

To estimate the distance to F1, we used the 3D dust reddening map of Green et al. (2019; hereafter "Bayestar19"), based on Gaia parallaxes and stellar photometry from the Panoramic Survey Telescope and Rapid Response System 1 (Pan-STARRS 1; Chambers et al. 2016) and Two Micron All Sky Survey (2MASS; Skrutskie et al. 2006). We accessed the Bayestar19 dust map with the `dustmaps`[19] Python package (v.1.0.6.) and made use of the associated online viewer.[20] The Bayestar19 map is measured in integrated color excess units of $E(g-r)$ assuming an optical extinction curve (Schlafly et al. 2016), which we convert to $E(B-V)$ via $E(B-V) = 0.981\,E(g-r)$ (Green et al. 2019).

Figure 13 (top) shows the Bayestar19 integrated dust reddening maps up to a distance of 300 pc (left) and 500 pc with the Planck I_{353} contours (white) overlaid (right). There is some indication of F1V in $E(B-V)$ at a distance of ∼300 pc, but we are only able to confidently identify F1K at a distance of ∼500 pc. We therefore assume a fiducial distance of $d = 500$ pc to F1. We note that this might somewhat overestimate the distance if our inability to identify F1 stems from a lack of Gaia stars with distance measurements rather than a lack of dust emission at ∼300 pc. There are insignificant changes in $E(B-V)$ for $d \gtrsim 500$ pc, and this approaches the Planck integrated dust map, suggesting that there is little dust emission beyond 500 pc. Our fiducial distance is roughly consistent with the Gaia-2MASS 3D dust extinction map (Lallement et al. 2019).

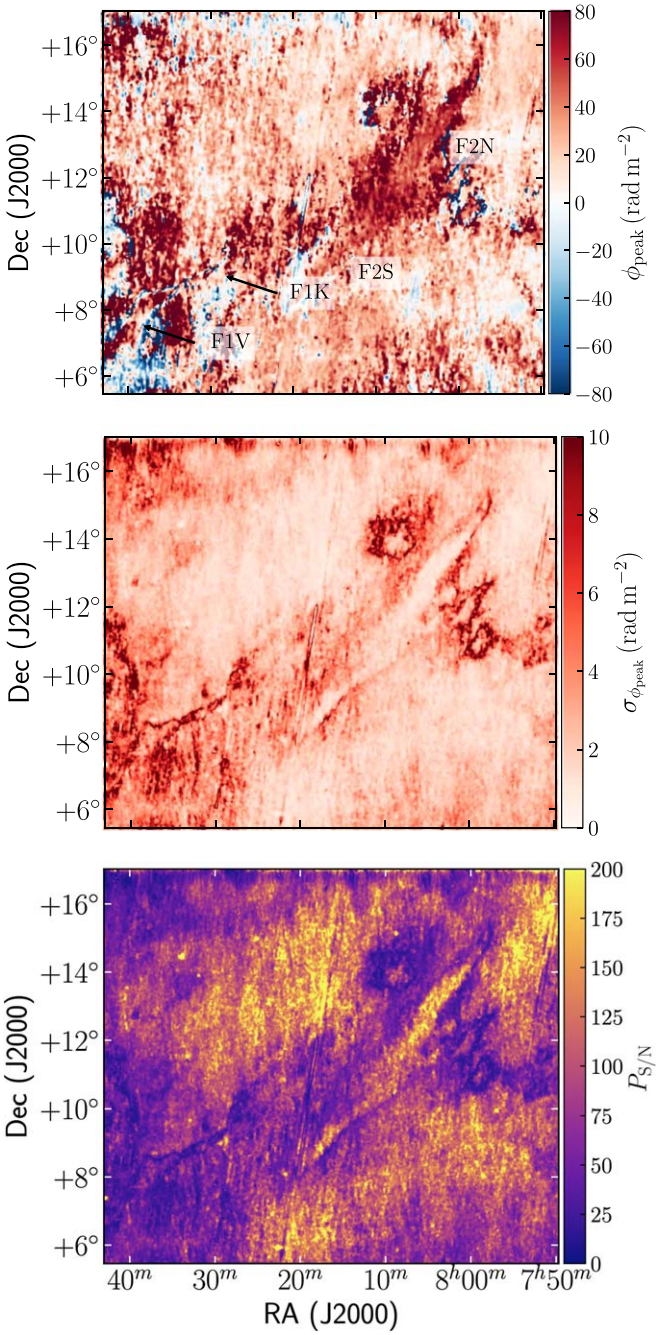

Figure 12. Gaussian fitting results of the cleaned GALFACTS Faraday depth spectra. Shown are maps of the peak Faraday depth $\phi_{\rm peak}$ (top), uncertainty in polarized intensity σ_P (middle), and S/N of the peak polarized intensity $P_{\rm S/N}$ (bottom). The locations of F1 and F2 as discussed in the text are indicated in the top panel.

Assuming a model of Galactic rotation, kinematic distance techniques use $v_{\rm lsr}$ measurements of H I to determine the distance to H I gas. We used a Monte Carlo kinematic distance code (Wenger et al. 2018) based on maser parallaxes and a universal Galactic rotation model (Reid et al. 2014) to estimate the kinematic distance to F1. With a peak F1K H I velocity

[19] https://dustmaps.readthedocs.io/en/latest/
[20] http://argonaut.skymaps.info/

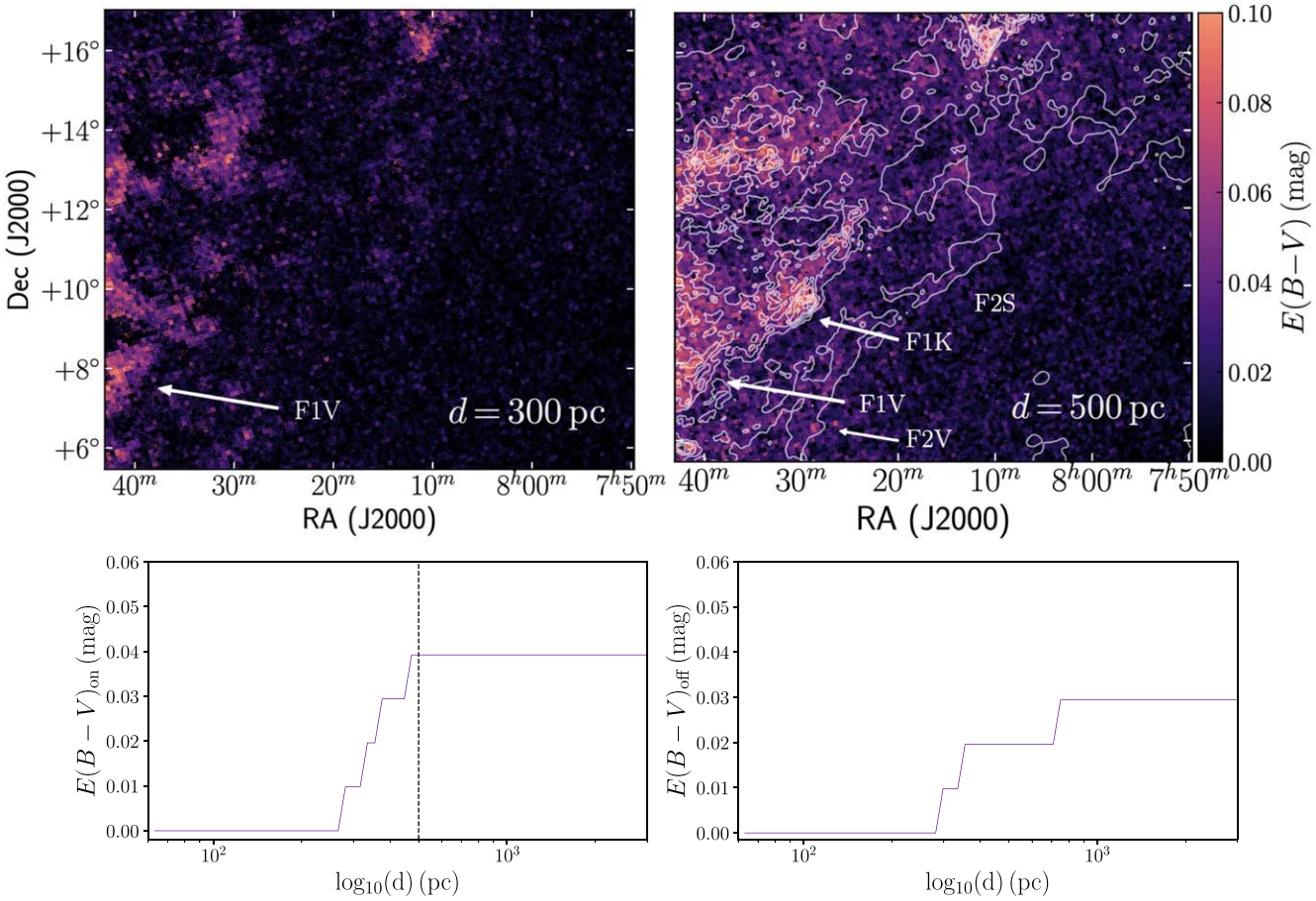

Figure 13. Bayestar19 dust reddening results of G216. Top: integrated $E(B-V)$ maps at a distance of 300 pc (left) and 500 pc, with the Planck I_{353} contours (white) overlaid representing values of 0.18, 0.24, 0.29, 0.35, 0.40, 0.45, 0.51, and 0.56 MJy sr^{-1} (right). The locations of F1 and F2 associated with dust emission as discussed in the text are indicated. Bottom: median $E(B-V)$ reddening profiles toward F1K for the "on" region (left), with our fiducial distance of 500 pc indicated with a dashed vertical line, and the "off" region (right).

$v_{\rm lsr} \sim +6\,{\rm km\,s^{-1}}$, we find a kinematic distance of 500^{+400}_{-320} pc that is consistent with our fiducial distance. At a distance of ∼500 pc, the vertical distance from the Galactic midplane is $\lesssim 300$ pc, so halo lag does not significantly affect our kinematic distance estimate and is ignored.

Figure 13 (bottom) shows the average Bayestar19 $E(B-V)$ profiles for the "on" (left) and "off" (right) regions along F1K. The spatial resolution of the data defines the number of profiles within our masks and is limited by the Gaia sampling of stars (Green et al. 2019). Both sets of reddening profiles show an increasing color excess over a similar distance range, suggesting that the dust emission is likely spatially coherent in this area.

5.2. Scaling with Path Length and Ionized Filling Factor

Several physical quantities of interest depend on parameters that cannot be unambiguously determined. The first of these is the LOS thickness through F1, referred to as the path length L. While the 3D geometry of the filament is unknown, we characterize the LOS path length as $L = Nw$, where N is the ratio of the LOS thickness of the filament to its apparent width on the sky w measured in pc. We measure an angular width of $\theta = 0.^{\circ}25$ of F1K in VTSS Hα emission, which, at our fiducial distance of 500 pc, corresponds to a physical width of $w = 2.2$ pc. The second parameter is the dimensionless ionized filling factor $f_{\rm ion}$, defined as the fraction of the path length that is occupied by ionized gas of uniform density. In light of this, we scale the following equations with $L_{2.2} \equiv L/(2.2\,{\rm pc})$ and $f_{\rm ion}$.

5.3. Emission Measure and Thermal Electron Density

The emission measure (EM) is estimated from the Hα intensity $I_{\rm H\alpha}$ following

$$\left(\frac{\rm EM}{\rm pc\ cm^{-3}}\right) = 2.75\left(\frac{T_{\rm WIM}}{10^4\ {\rm K}}\right)^{0.9}\left(\frac{I_{\rm H\alpha}}{\rm R}\right)\left(\frac{\tau_{\rm int}}{1-e^{-\tau_{\rm int}}}\right)e^{\tau_{\rm fg}} \quad (6)$$

(Reynolds 1988), where we assume a WIM temperature of $T_{\rm WIM} \sim 0.8 \times 10^4$ K (Haffner et al. 1998) and $I_{\rm H\alpha}$ is measured in R. There are two correction terms for the dust optical depth, including contributions of the foreground dust, $\tau_{\rm fg}$, and those of the dust mixed in with the Hα emission, $\tau_{\rm int}$ (Finkbeiner 2003), which does not include the foreground contribution. We use the Planck $E(B-V)$ map of the diffuse, high-Galactic-latitude sky (Planck Collaboration et al. 2014). We measured the foreground contribution using the "off" region, while the internal contribution was measured using the "on" minus "off" region, corresponding to $E(B-V)_{\rm fg} = 0.034 \pm 0.004$ mag and $E(B-V)_{\rm int} = 0.020 \pm 0.017$ mag, respectively. The dust

optical depths were derived using

$$\tau = \left(\frac{2.65}{1.086}\right) E(B-V) \quad (7)$$

(Finkbeiner 2003), where the factor of 2.65 describes the shape of the extinction curve and the factor of 1.086 converts the color excess to dust optical depth. This yields foreground and internal dust optical depths, respectively, of $\tau_{\rm fg} = 0.084 \pm 0.009$ and $\tau_{\rm int} = 0.05 \pm 0.04$.

We used the Planck color excess map over that of Bayestar19 owing to its more complete spatial coverage, although both give similar results. These dust extinction corrections assume that there is no dust emission behind F1K, resulting in an upper limit of EM. At these Galactic latitudes, it is reasonable to assume that most of the dust is foreground to F1. This is consistent with our results in Section 5.1, where we found insignificant changes in $E(B-V)$ at distances beyond 500 pc.

The thermal electron density is related to the EM via

$$\left(\frac{n_e}{\rm cm^{-3}}\right) = \frac{1}{\sqrt{2.2}}\left(\frac{\rm EM}{\rm pc\ cm^{-6}}\right)(f_{\rm ion}L_{2.2})^{-0.5}, \quad (8)$$

assuming that the ionized plasma is distributed in clumps of uniform density filling a total length $f_{\rm ion}L_{2.2}$, called the occupation length. We find an Hα intensity $I_{\rm H\alpha} = 2.2 \pm 0.8$ R, EM $= 6 \pm 2$ pc cm^{-6}, and $n_e = (1.5 \pm 0.3)(f_1 L_{2.2})^{-0.5}$ cm^{-3}.

5.4. Magnetic Field Strength

The LOS magnetic field strength can be estimated by introducing $L_{2.2}$ and $f_{\rm ion}$ to Equation (4),

$$\left(\frac{B_\parallel}{\mu\rm G}\right) = \frac{1}{(0.81)(2.2)}\left(\frac{\rm RM}{\rm rad\ m^{-2}}\right)\left(\frac{n_e}{\rm cm^{-3}}\right)^{-1}(f_{\rm ion}L_{2.2})^{-1}. \quad (9)$$

Similar to Equation (8), this assumes an occupation length $f_{\rm ion}L_{2.2}$ for the ionized plasma through which the magnetic field is threaded. We make use of our map of $\phi_{\rm peak}$ from Section 4.6, measuring a Faraday depth of $\phi = +19 \pm 13$ rad m^{-2}. This, along with our measurements of EM from the previous section, yields an LOS magnetic field strength of $B_\parallel = (+6 \pm 4)(f_{\rm ion}L_{2.2})^{-0.5}$ μG. Since the measured EM and n_e are upper limits, $B_\parallel$ is a lower limit.

5.5. Plasma Beta

The relative importance of magnetic energy can be quantified using the ratio of thermal gas ($P_{\rm th}$) to magnetic ($P_{\rm mag}$) pressure, commonly referred to as the plasma beta parameter,

$$\beta = \frac{P_{\rm th}}{P_{\rm mag}}. \quad (10)$$

To reflect the observed spatial separation between the ionized and neutral medium along F1K, we assume that the thermal gas pressure is dominated by ionized gas,

$$\left(\frac{P_{\rm th}/k_B}{\rm K\ cm^{-3}}\right) = 2\left(\frac{n_e}{\rm cm^{-3}}\right)\left(\frac{T_{\rm WIM}}{\rm K}\right), \quad (11)$$

Table 1
Assumptions and Observational Results of Our Quantitative Analysis for F1K.

Parameter	Assumptions	Value
d		500 pc
$f_{\rm ion}$		1.0
$T_{\rm WIM}$		8000 K (Haffner et al. 1998)
	Observables	
θ		0.25°
$I_{\rm H\alpha}$		2.2 ± 0.8 R
$E(B-V)_{\rm fg}$		0.034 ± 0.004 mag
$E(B-V)_{\rm int}$		0.020 ± 0.017 mag
$\phi_{\rm peak}$		$+19 \pm 13$ rad m^{-2}

Note. Here d is the LOS distance, $f_{\rm ion}$ is the ionized filling factor, $T_{\rm WIM}$ is the WIM gas temperature, θ is the angular width, $I_{\rm H\alpha}$ is the Hα intensity, $E(B-V)_{\rm fg}$ is the foreground color excess, $E(B-V)_{\rm int}$ is the internal color excess, EM is the emission measure, and $\phi_{\rm peak}$ is the peak Faraday depth.

where k_B is the Boltzmann constant. We again assume a WIM temperature of $T_{\rm WIM} \sim 0.8 \times 10^4$ K (Haffner et al. 1998). The contribution of gas pressure from the neutral medium is approximately an order of magnitude lower than that of the ionized medium and does not significantly affect our results. This yields a thermal gas pressure of $P_{\rm th}/k_B = (2.5 \pm 0.5) \times 10^4 (f_{\rm ion}L_{2.2})^{-0.5}$ K cm^{-3}.

The magnetic pressure is determined via

$$\left(\frac{P_{\rm mag}/k_B}{\rm K\ cm^{-3}}\right) = \frac{1}{8\pi}\left(\frac{B_{\rm tot}}{\mu\rm G}\right)^2, \quad (12)$$

where $B_{\rm tot}$ is the total field strength in μG. The 3D magnetic field geometry of F1, which sets the relationship between $B_\parallel$, $B_\perp$, and $B_{\rm tot}$, is unknown. However, it is unlikely that the total magnetic field of F1 is predominantly along the LOS, implying that $B_{\rm tot} > B_\parallel$. While we use the estimate of $B_\parallel$ for $B_{\rm tot}$, we note that this underestimates the magnetic field strength and correspondingly overestimates plasma beta.

We find a magnetic pressure $P_{\rm mag}/k_B = ([1.1^{+1.5}_{-1.1}] \times 10^4)(f_{\rm ion}L_{2.2})^{-0.5}$ K cm^{-3} and plasma beta $\beta = (2.1^{+3.1}_{-2.1})(f_{\rm ion}L_{2.2})^{-1}$.

6. Discussion

6.1. Physical Interpretation

We consider two possible 3D geometries for F1: (I) a filament and (II) an edge-on sheet. For (I), we set the path length equal to the filament width. Assuming that the filament makes an angle of 60° with the LOS, the median value for a random distribution, this corresponds to a ratio of path length to apparent width on the sky of $N = 1.2$. For (II) we assume $N = 15$ such that the resulting path length is approximately equal to the ~ 30 pc typical scale length of the WIM (Ferrière 2020). Since the H I emission is not coincident with the ionized filament, we adopt a filling factor of $f_{\rm ion} = 1.0$. We find that the internal pressure of F1 (discussed below) can be explained using a filament geometry. With no strong evidence to suggest that this structure is sheet-like, we adopt a filament geometry for F1. Our assumptions and observables are summarized in Table 1.

Table 2
Physical Parameters Derived for F1K with a Comparison of Similar Studies from the Literature

	This Work	Other Work			
	F1K of G216	3C 196[a]	Sh 2-27 NC[b]	Sh 2-27 FC[b]	IVF[c]
L (pc)	2.6 ($N = 1.2$)	1.5×10^3	∼30	∼30	18 ± 9
n_e (cm^{-3})	1.5 ± 0.3	∼0.03	∼0.02	∼0.02	∼0.2
$B_\parallel$ (μG)	$+6 \pm 4$	$+0.3 \pm 0.1$	~ -15	∼+30	2.8 ± 0.8
β	$2.1^{+3.1}_{-2.1}$	31 ± 21[d]	∼0.08[e]	∼0.02[e]	∼0.1–1

Notes. Here L is the path length, n_e is the thermal electron density, $B_\parallel$ is the LOS magnetic field strength, and β is the plasma beta.
[a] Diffuse LOFAR field (Jelić et al. 2015).
[b] Dust clouds foreground to the Sharpless 2-27 (Sh 2-27) H II region with a near-cloud (NC) and far-cloud (FC) component (Thomson et al. 2019).
[c] Intermediate-velocity filament (IVF; Stil & Hryhoriw 2016).
[d] Computed here assuming $f_{\rm ion} = 1$, $T_{\rm WIM} = 8 \times 10^3$ K, and $B_{\rm tot} \sim \sqrt{3} B_\parallel$.
[e] Computed here assuming $f_{\rm ion} = 10^{-3}$, $T_{\rm CNM} = 80$ K, and $B_{\rm tot} \sim \sqrt{3} B_\parallel$.

We find a thermal electron density $n_e = 1.5 \pm 0.3\,{\rm cm}^{-3}$, an LOS field strength $B_\parallel = 6 \pm 4\,\mu$G, and plasma beta $\beta = 2.1^{+3.1}_{-2.1}$. The thermal electron density is roughly one order of magnitude higher than what is typically found in the diffuse WIM (e.g., Ferrière 2001; Gaensler et al. 2008). The magnetic field strength of F1 may help to stabilize it against thermal pressure, and a significant $B_\perp$ component would reduce β toward a more magnetically dominated regime. Our model-dependent results are shown in Table 2.

We estimate the theoretical synchrotron intensity of F1 to determine whether our estimate of the magnetic field strength is consistent with the lack of correlated excess synchrotron emission in the GALFACTS data (recall Figure 1). The GALFACTS total intensity data have not been calibrated to a stable zero-point due to scanning artifacts (Leahy 2018). For this reason, we used reprocessed 1.4 GHz continuum data from the HI Parkes All-Sky Survey (CHIPASS; Calabretta et al. 2014).

The synchrotron total intensity depends on $B_\perp$ and the cosmic-ray density $n_{\rm cr}$ via

$$I \propto \int B_\perp^{\frac{p+1}{2}} n_{\rm cr}\, d\ell, \tag{13}$$

where $p = 3$ is the spectral index of the cosmic-ray distribution (Jaffe et al. 2010). We measured the ratio of the expected synchrotron intensity from F1 to that of the Galactic background, $I_{\rm F1}/I_{\rm MW}$, assuming $B_\perp \sim B_\parallel$, a constant $n_{\rm cr}$ along the LOS, a typical Galactic magnetic field strength of $\sim 6\,\mu$G (Rand & Kulkarni 1989) projected to the POS of $(2/\sqrt{3})6\,\mu$G, and a Galactic synchrotron path length of ~ 10 kpc in this direction (Sun et al. 2008). This yields the quantity $I_{\rm F1}/I_{\rm MW} \sim 2 \times 10^{-4}$, which can be multiplied by the local background synchrotron intensity to yield $I_{\rm F1}$. We find an average value of $I_{\rm MW} \sim 3.5$ K in the direction of G216, yielding a theoretical value of $I_{\rm F1} \lesssim 1$ mK that is roughly equal to the rms uncertainty in the GALFACTS Stokes I map. Therefore, the magnetic field strength that we measure does not necessitate a corresponding detectable structure in the GALFACTS total intensity.

Magnetic field alignments between different ISM phases are to be expected in regions where dynamical events such as supernova explosions, stellar winds, and expanding H II regions have swept up the ambient medium. Such events can lead to cavities in the ISM identified as H I shells, where the swept-up material is contained in the cavity wall (e.g., McClure-Griffiths et al. 2003). In light of G216 being found at the northern edge of a large, low column density region seen in both Hα and dust emission, we consider the possibility that this region is related to a shell or bubble in the ISM.

The IVC H I gas at $v_{\rm lsr} \lesssim -20\,{\rm km\,s}^{-1}$ contains finger-like projections directed toward the Galactic plane (Figure 2, top left) that strongly resemble Rayleigh–Taylor instabilities found along the walls of Galactic H I shells (e.g., Dawson et al. 2011; McClure-Griffiths et al. 2003). We searched catalogs of known H I shells near this part of the outer Galaxy (Heiles 1979; Hu 1981; Heiles 1984) and found no previously identified shell that is morphologically associated with G216. Using data from the all-sky H I 4π (HI4PI) survey (HI4PI Collaboration et al. 2016) based on EBHIS (Winkel et al. 2016) and the Parkes Galactic All-Sky Survey (GASS; McClure-Griffiths et al. 2009; Kalberla et al. 2010; Kalberla & Haud 2015), we inspected the H I structure in velocity channel maps to search for evidence of an H I shell. Based on the criteria described by McClure-Griffiths et al. (2002), we find no strong evidence of the existence of an H I shell. The morphology of 353 GHz Planck dust polarization data can be used to identify a swept-up shell wall (e.g., Soler et al. 2018); however, we do not find strong evidence for a large-scale shell in the Planck dust magnetic field orientation.

Despite the lack of evidence for an H I shell, we consider the possibility of a recently propagated shock through this region. Using soft X-ray data from the all-sky ROSAT survey (Snowden et al. 1997) over the energy range 0.1–2.4 keV, we searched for excess X-ray emission associated with G216. We measured an average X-ray count consistent with zero photons per pixel, finding no evidence of X-ray emission that is spatially correlated with the structures discussed in this paper.

We used the X-ray spectral fitting program `xspec` (Arnaud 1996), accessed with the online tool `WebSpec`,[21] to model the expected X-ray photon count of a typical shock propagating through this region. `WebSpec` assumes an absorbing foreground column $N_{\rm H\,I}$, thermal electron density n_e (which we assume to be equal to the H I density), plasma temperature T_p, and radius R of the emitting region. Based on our measurements in Section 5, we converted the foreground dust optical depth $\tau_{\rm fg}$ to a foreground H I column density of

[21] https://heasarc.gsfc.nasa.gov/webspec/webspec.html

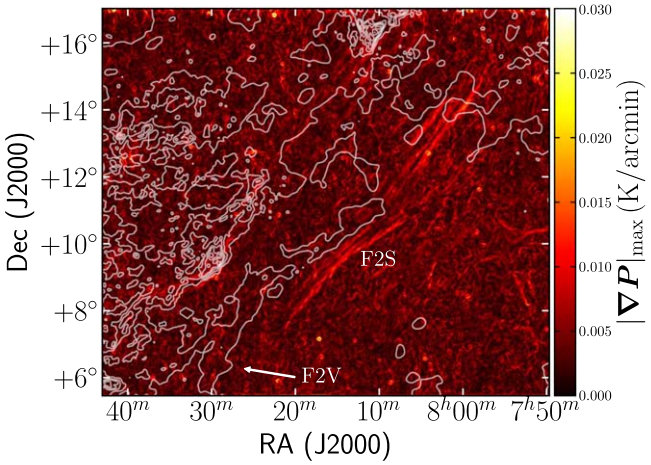

Figure 14. GALFACTS $|\nabla P|_{\max}$ of G216 at 5′ resolution with the same Planck I_{353} contours as Figure 13 overlaid (white). The locations of F2 associated with dust emission as discussed in the text are indicated.

$N_{\rm H\,I} = 1.9 \times 10^{20}\,{\rm cm}^{-2}$. We assume a radius corresponding to an angular size of 10°, roughly equal to the size of the low column density region toward G216, at our fiducial distance of 500 pc. We measured an expected X-ray count that is roughly consistent with little to no average X-ray emission per ROSAT pixel over a range in electron density $2 \times 10^{-3}\ {\rm cm}^{-3} < n_e < 0.01\,{\rm cm}^{-3}$ and plasma temperature $10^5\ {\rm K} < T_p < 10^7\,{\rm K}$. This is likely due to the absorbing foreground H I; without it, we find average X-ray photon counts that are several orders of magnitude higher. We are therefore unable to rule out the possibility of a previous shock. If a shock did occur, this could have triggered the formation of dense CNM gas adjacent to F1K, where several dense clumps are found.

6.2. Multiphase Structure of F1 and F2

The F1 polarization gradient filament has clear associations with tracers of the multiphase ISM. While F1 is spatially correlated with a small-scale VTSS filament, it is possibly embedded in the more extended WHAM filament. The $\sim 2°$-wide depolarized band between F1 and F2 in the GALFACTS data is spatially correlated with extended WHAM emission along the edge of the diffuse ionized and neutral gas emission. This suggests that the small-scale Hα filament may be associated with the edge of a larger, more diffuse structure. The spatial separation between the ionized and neutral media along F1K suggests an ionized layer around a neutral gas cloud. The ionized layer of F1 is spatially offset from the neutral cloud in the direction toward the Galactic plane, where the photoionizing flux from, e.g., massive OB stars is expected to be higher.

While F1 is spatially correlated with a bright Hα filament and a sharp edge in the H I column density and Planck dust emission, the correspondences between F2 and other ISM tracers are subtler. Careful inspection of the VTSS and WHAM data reveals that F2 is spatially correlated with edges of very faint Hα emission. This is reminiscent of small-scale structures in the polarization gradient ascribed to turbulence-driven fluctuations that were too faint to be observed in Hα emission (Gaensler et al. 2011). Numerical simulations of magneto-hydrodynamic (MHD) turbulence reproduce extended filamentary structures in the polarization gradient similar to those found in real data (e.g., Iacobelli et al. 2014), suggesting that F2 and similar structures are an expected consequence of turbulence.

Despite the lack of H I or dust emission spatially coincident with F2, there is a filament in the neutral ISM that extends along the eastern edge of F2S with a similar curvature. Figure 14 shows the GALFACTS polarization gradient (red) with Planck I_{353} dust emission contours overlaid (white), clearly showing the alignment. This dust filament strongly resembles an H I filament in the local gas at velocities $+4$ km s$^{-1} \lesssim v_{\rm lsr} \lesssim +20$ km s^{-1}. The strong morphological similarity but lack of spatial coincidence between the neutral filament and F2S suggests an ionized−neutral boundary along F2.

6.3. Comparison to Other Studies

We compare our results to radio polarization studies of discrete structures in the high Galactic latitude diffuse/translucent ISM, restricting this to a few studies.

The 3C 196 LOFAR field contains polarized intensity structures that are aligned with the Planck dust POS magnetic field direction (Jelić et al. 2015). Assuming that the observed RM is produced by the WIM over a path length of 1.5 kpc, the authors find $\langle B_\parallel \rangle = 0.3 \pm 0.1\ \mu$G. The estimated $\langle n_e \rangle$ is lower than typical values for the diffuse WIM and our results for F1 by roughly one and two orders of magnitude, respectively. Based on models of the GMF (Sun et al. 2008), the authors note that the regular magnetic field is primarily in the POS toward this direction. The same GMF models predict both large-scale LOS and POS magnetic field components toward G216, consistent with our observations. The authors suggest that a prominent, polarized filamentary structure in 3C 196 is an ionized filament wrapped around neutral H I gas, similar to our interpretation of the ionized layer of F1. In Section 6.5, we discuss the possibility that LOFAR polarized intensity structures trace the predominantly neutral, rather than ionized, ISM.

The foreground Faraday rotation toward the nearby H II region Sharpless 2-27 (Sh 2-27) was modeled using data from the 64 m Parkes Radio Telescope as part of the Global Magnetoionic Medium Survey (GMIMS; Wolleben et al. 2009; Thomson et al. 2019). This revealed near-cloud (NC) and far-cloud (FC) components with $B_\parallel \sim -15\ \mu$G and $B_\parallel \sim +30\ \mu$G, respectively, over equal path lengths of ~ 30 pc. These foreground clouds are interpreted as CNM-bearing dust clouds that dominate the RM along the LOS. Assuming $T_{\rm CNM} = 80$ K and an ionization fraction $\sim 10^{-3}$ (Ferrière 2020) for the CNM and $B_{\rm tot} \sim \sqrt{3}\,B_\parallel$, we find that the NC and FC components have magnetically dominated plasma betas of $\beta \sim 0.08$ and $\beta \sim 0.02$, respectively.

Stil & Hryhoriw (2016) investigated the magnetic properties of an ionized intermediate-velocity Hα filament (designated as IVF here) in VTSS (Finkbeiner 2003) and WHAM (Haffner et al. 2003) data. Using RM measurements based on National Radio Astronomy Observatory VLA Sky Survey (NVSS) data (Taylor et al. 2009), excess RM is found to be spatially correlated with extended WHAM emission. This is in contrast to our results of F1, where we find an excess RM that is correlated with the small-scale VTSS filament. Using an empirical relationship between the EM and dispersion measure (Berkhuijsen et al. 2006), the authors find $B_\parallel = 2.8 \pm 0.8\ \mu$G and $\beta \sim 0.1$–1. The authors conclude that their IVF is completely ionized and magnetically dominated, similar to our results of F1.

These radio polarization studies (summarized in Table 2) highlight the importance of magnetic fields in structuring the high-Galactic-latitude ISM. Magnetic fields play an important role in shaping both discrete ionized and neutral structures in the diffuse/translucent ISM. However, it remains unclear whether and how the magnetic field in these phases are associated, emphasizing the need for further multiphase magnetic field analyses.

6.4. Multiphase Magnetic Field Comparison

The alignment found between GALFACTS polarization gradient filaments and narrow GALFA-H I structures across a wide velocity range suggests that the ionized gas and neutral gas share a common magnetic field in this region. Since the structures analyzed in this paper are not spatially correlated with excess synchrotron emission, we are unable to derotate the synchrotron polarization angles to directly compare magnetic field orientations in the ionized and neutral medium. The observed synchrotron polarization angles, however, provide information about the combination of magnetic field orientation and Faraday rotation. If the observed polarization angle is coherent, either the magnetic field orientation and degree of path-length-integrated Faraday rotation is constant as a function of position, or these two quantities change in the amount required to yield no net change in the observed polarization angle. While the latter is possible, the former is more plausible. The strong degree of coherence in the observed GALFACTS polarization angles in Figure 7 highlights large areas of this region where the path-length-integrated LOS magnetic field orientation in the ionized gas is roughly constant. This is supported by the roughly constant $\phi_{\rm max}$ that we measure toward these LOSs. Comparison with the dust polarization data in Figure 5 (left) suggests that the POS field component is also strongly coherent.

We showed that F1 may be a magnetically dominated ionized filament. Significant magnetic pressure would prevent gas flow perpendicular to the filament, resulting in a magnetic field in the ionized medium that is parallel to F1 (e.g., Stil & Hryhoriw 2016). If the Hα filament is magnetically dominated, the alignment that we find with the Planck dust POS magnetic field orientation and narrow H I structures would support our interpretation of multiphase magnetic field alignment.

If the ionized medium and neutral medium do share a common magnetic field, it is reasonable to expect that they have consistent magnetic field directions and comparable field strengths. Zeeman splitting measurements can be used to measure the LOS magnetic field direction and strength in cold neutral gas. We identified a Zeeman splitting measurement using H I absorption (Heiles & Troland 2004) toward a single LOS at the far east of our field at coordinates $(\ell,\ b) = (213^\circ,\ +30.1^\circ)$ with two magnetic field strength estimates: $-1.9 \pm 2.2\ \mu$G and $-3.2 \pm 3.7\ \mu$G. While the magnetic field direction measured using Zeeman splitting is negative, the sign convention is opposite to that of RM (Robishaw & Heiles 2021), resulting in a consistent magnetic field direction between the ionized and neutral gas along this LOS.

To compare our magnetic field strength estimates in the ionized gas to that of the predominantly neutral medium, we apply the Davis–Chandrasekhar–Fermi (DCF) method (Davis 1951; Chandrasekhar & Fermi 1953) to the 80′ Planck dust polarization angles, $\tilde{\chi}_{353}$, to measure the total magnetic field strength. We use the form of the DCF as modified by Heitsch et al. (2001),

$$\langle B \rangle^2 = \xi 4\pi\rho \frac{\sigma_v^2}{\sigma(\tan\delta_\chi)^2}, \tag{14}$$

where σ_v is the turbulent line width, ρ is the mass density of the neutral medium, $\xi = 0.5$ is a correction factor that reflects the ratio of turbulent magnetic to turbulent kinetic energy, and δ_χ is the dispersion in dust polarization angle from the mean value given by $\delta_\chi \equiv \chi_{353} - \langle\chi_{353}\rangle$.

To apply the DFC method to F1, we used the same "on" mask in Section 5 at 5′ resolution for use with the H I data and degraded to 80′ resolution for the dust polarization data. Assuming a filamentary geometry of F1 with a path length of 2.2 pc (Section 6.1), we measured an H I number density of $n_{\rm H\,I} = N_{\rm H\,I}/2.2\ {\rm pc} \sim 10\ {\rm cm}^{-3}$ over a velocity range 0 km s^{-1} $\lesssim v_{\rm lsr} \lesssim +10$ km s^{-1} using Equation (2). This corresponds to a mass density of $\rho = 1.4 m_H n_{\rm H\,I} = 2 \times 10^{-23}\ {\rm g\ cm}^{-3}$. We assumed that $\sigma_v = \sigma_{\rm turb} = 1.4\ {\rm km\ s}^{-1}$, where $\sigma_{\rm turb}$ is the turbulent velocity (McClure-Griffiths et al. 2006; Clark et al. 2014), found to be equal to the CNM component of F2 found with ROHSA. We find a dust polarization angle dispersion of $\delta_\chi \sim 5^\circ$, yielding a total magnetic field strength of $\sim 21\ \mu$G in the neutral medium, which may only be accurate to within a factor of a few (McClure-Griffiths et al. 2006; Yoon & Cho 2019; Cho & Yoo 2016; Skalidis et al. 2021). While this is higher than the total magnetic field strength in the ionized gas inferred from our Faraday depth measurements, $B_{\rm tot} \sim 6 \pm 4\ \mu$G, this is consistent with increased magnetic field strengths found in the predominantly neutral medium (e.g.,Wolleben et al. 2009; Crutcher et al. 2010; McClure-Griffiths et al. 2006; Clark et al. 2014; Tritsis et al. 2019; Thomson et al. 2019). The magnetic field strength that we estimate using the DFC method along F1 is also higher than that of the far east of our field away from the filament found using Zeeman splitting measurements, further suggesting magnetic field compression along F1.

Our ROHSA results (Section 4.3) suggest that we may be seeing a magnetic field alignment between the WNM and CNM. While we identify narrow H I structures over an H I velocity range of -20 km s^{-1} $\lesssim v_{\rm lsr} \lesssim +20$ km s^{-1} for the entire region, the WNM is found to dominate the H I emission outside of the velocity range -10 km s^{-1} $\lesssim v_{\rm lsr} \lesssim 0$ km s^{-1} toward the small portion of F2 that we analyze. If the WNM dominates narrow H I structures in a similar velocity range in the rest of G216, then the roughly coherent H I orientation over the ~ 40 km s^{-1} velocity range (Figure A.1) may reflect a common POS magnetic field orientation in the WNM and CNM. A more complete ROHSA analysis on the entire field is required to further understand over what velocity range the CNM and WNM dominate narrow H I structures.

6.5. Interpreting Spatial Correlations between Radio Polarization Structures and H I Emission

Spatial correlations found between radio polarization structures and H I emission can be interpreted in two ways. Either the ionized and neutral media, and potentially their magnetic fields, are correlated, or the polarized emission is dominated by emission from the H I structure itself. We discuss the two possibilities here.

Faraday rotation by the multiphase ISM has significant implications for the interpretation of radio polarimetric

observations, particularly at low frequencies. Faraday rotation is linearly proportional to n_e and typically discussed as an effect from the WIM (e.g., Haverkorn et al. 2004a, 2004b; Hill et al. 2008; Gaensler et al. 2011; Heiles & Haverkorn 2012). Assuming a typical local thermal electron density and $B_\parallel = 2\,\mu$G, Van Eck et al. (2017) showed that the WIM produces an amount of Faraday rotation per unit path length of $\sim 0.32\,\mathrm{rad\,m^{-2}\,pc^{-1}}$, while the WNM and HIM only produce ~ 0.016 and $\sim 0.008\,\mathrm{rad\,m^{-2}\,pc^{-1}}$, respectively. A similar estimate for the CNM, assuming an electron density of $n_e \sim 0.02\,\mathrm{cm^{-3}}$ (Ferrière 2020) and the same LOS magnetic field strength, yields $\sim 0.03\,\mathrm{rad\,m^{-2}\,pc^{-1}}$ (Thomson et al. 2019). As a result, observable Faraday rotation from phases other than the WIM requires significant LOS magnetic field strengths and/or path lengths. The typical length scale of the CNM is ~ 10 pc (Ferrière 2020), rendering significant path lengths unlikely. Increased magnetic field strengths have been shown to produce measurable Faraday rotation in CNM-associated dust clouds (Thomson et al. 2019) and in molecular clouds (Tahani et al. 2018).

The 3C 196 LOFAR field (van Haarlem et al. 2013) contains radio polarized structures that are spatially aligned with the dust POS magnetic field orientation in Planck dust polarization (Jelić et al. 2015; Zaroubi et al. 2015). Recent work by Bracco et al. (2020) found spatial correlations between LOFAR polarized intensity structures and H I emission using data from the Effelsberg–Bonn H I Survey (EBHIS) toward the 3C 196 field, hypothesizing that this observational correlation may be due to Faraday rotation from the CNM. However, Van Eck et al. (2017) showed that at the very low LOFAR frequencies ($\sim$150 MHz), Faraday rotation from the WIM causes significant depth depolarization, resulting in polarized intensity structures dominated by the Faraday-thin neutral ISM. Furthermore, the existence of LOFAR polarization structures aligned with cold H I emission alone is not evidence for a significant RM contribution from the CNM. Strong evidence for Faraday rotation from the CNM would require a correlation between cold H I gas and RM structures signifying enhanced Faraday rotation. The observed correlation found by Bracco et al. (2020) is consistent with the explanation provided by Van Eck et al. (2017) and therefore does not constitute evidence that CNM provides a significant contribution to the measured RM toward 3C 196. The results of Van Eck et al. (2017) suggest that the spatial correlation between LOFAR polarized intensity structures and the Planck dust magnetic field orientation presented by Jelić et al. (2015) reflects a common magnetic field orientation in the predominantly neutral ISM.

Spatial correlations found between LOFAR depolarization canals, cold H I structures, and POS magnetic field orientation in Planck dust emission have been described as another example of multiphase magnetic field alignment (Jelić et al. 2018; Turić et al. 2021). The small spatial scale of these depolarization canals indicates that they are likely caused by beam depolarization, where fluctuations in the observed polarization angle become averaged within the telescope beam. The fluctuation in the observed polarization angle may be caused either by changes in the degree of foreground Faraday rotation or by changes in the intrinsic magnetic field orientation within the polarized emitting region. If changes in the foreground RM are responsible for these canals, they are likely to be WIM-dominated structures, and their alignment with tracers of the magnetized neutral ISM may be evidence for multiphase magnetic field alignment. However, if these canals trace changes in the intrinsic magnetic field orientation, they are likely to be neutral-dominated structures, and the observed alignment of magnetic field tracers may again reflect a common field orientation in the neutral medium.

The Faraday rotation presented in this paper is likely a consequence of ionized gas. The RM excess of F1 is spatially coincident with an Hα filament and is clearly offset from the edge of H I and dust emission, rendering Faraday rotation from within the neutral medium unlikely. The RM enhancement toward F2 is also found to be spatially correlated with very faint Hα emission. Assuming typical thermal electron densities and $B_\parallel = 6\,\mu$G (Section 6.1), the WIM and CNM are expected to produce an amount of Faraday rotation per unit path length of 0.97 and $0.097\,\mathrm{rad\,m^{-2}\,pc^{-1}}$, respectively. With an enhanced RM of $\sim 40\,\mathrm{rad\,m^{-2}}$ toward F2, this requires a WIM and CNM path length of $\sim$40 and $\sim$400 pc, respectively. This is typical of the length scale of the WIM but roughly one order of magnitude greater than that of the CNM (Ferrière 2020). The 1.4 GHz GALFACTS polarization data have a maximum Faraday depth scale that is ~ 30 times greater than that of LOFAR (Van Eck et al. 2017) and is therefore less severely depolarized by the WIM; while the observing frequency can strongly affect the interpretation of polarized intensity structures, Faraday rotation generally remains dominated by ionized gas. The comparison of GALFACTS polarization structures and H I emission presented in this paper is therefore a comparison of two tracers that genuinely trace different phases of the ISM.

6.6. Why Are Associations between Multiphase Magnetic Field Tracers Not More Widespread?

Multiphase structures and their magnetic fields are not widely associated. Van Eck et al. (2019) compared Faraday depth cubes from the LOFAR Two-meter Sky Survey (LOTSS; Shimwell et al. 2017), covering 568 deg^2 of the high Galactic latitude sky, to other multifrequency tracers, finding only one LOFAR filament that is spatially correlated with H I emission (see their Figure 11). Their H I filament lies along the boundary of a linear gradient in Faraday rotation, suggested to be due to an envelope of ionized gas surrounding the predominantly neutral H I filament. Of the four targeted studies that compared LOFAR polarized intensity structures to H I emission (Jelić et al. 2015; Bracco et al. 2020), only two showed strong morphological correlations. If LOFAR polarized intensity structures are dominated by Faraday-thin structures in cold gas (Van Eck et al. 2017), the lack of global spatial correlations with H I emission only further demonstrates the complexity of radio polarization studies. For instance, the polarization horizon of LOFAR is significantly closer than that of GALFACTS and may not sample the full polarized-emitting Galactic volume. More recently, Ogbodo et al. (2020) compared magnetic field strengths derived using OH masers as part of the Mapping the Galactic Magnetic field through OH masers (MAGMO) project (Green et al. 2012) with pulsar Faraday rotation measurements collated from Nota & Katgert (2010). These measurements probe the neutral and ionized medium, respectively, and were chosen toward H II regions that should dominate the environment in both tracers. While the statistics are limited and do not necessarily reflect the large-scale GMF properties, they found no strong correlation between these magnetic field measurements.

The alignment found between GALFACTS polarization gradient filaments and GALFA-H I structures presented in this paper is not a widespread occurrence in the high Galactic latitude Arecibo sky. The polarization gradient filaments analyzed here are highly coherent and significantly isolated from other, more complex structures in the polarization gradient compared to those typically found in the GALFACTS data. It may be that polarization gradient and H I emission structures are widely correlated, but observational effects make observing them difficult. Alternatively, associations between warm ionized and cold neutral gas physically may only exist in rare circumstances.

An important observational effect is the polarization horizon, the distance beyond which polarized emission is completely depolarized (Uyaniker et al. 2003). The distance to the polarization horizon is given by

$$D_{\rm ph} = \frac{\pi}{0.81 \lambda^2 n_e B_\parallel}, \quad (15)$$

resulting in polarized intensity structures that generally sample varying Galactic volumes as a function of observing frequency that also depends on angular resolution and direction. Assuming mean values of $B_\parallel \sim 2\ \mu$G and $n_e \sim 0.02\ {\rm cm}^{-3}$, the distance to the GALFACTS polarization horizon is $D_{\rm ph} \sim 2$ kpc, a factor of ~ 5 smaller than the total path length in this direction (Sun et al. 2008). The distance to the polarization horizon as given in Equation (15) is for the idealized case of a uniform medium, and its true distance is likely much less than this owing to turbulence. Even if there is widespread multiphase magnetic field alignment, the GALFACTS polarization horizon may render them unobservable and could help to explain the lack of observed alignments. The polarization horizon is not a well-defined boundary in distance, and information beyond the polarization horizon may still affect observables (Hill 2018).

An alignment between structures in the polarization gradient and narrow H I structures necessitates both an LOS magnetic field component in the ionized medium and a POS magnetic field component in the neutral medium, respectively, and may therefore be unlikely to occur in regions that contain predominantly ionized or neutral gas. Our visual comparison of polarization gradient filaments in the Arecibo data and other multifrequency tracers revealed that there is not a one-to-one correspondence between polarization gradient and Hα filaments. Some examples of this in G216 include the F1V structure that is prominently observed in VTSS Hα emission but not in the 5′ polarization gradient, and the filamentary F2 structure that is prominently seen in the 5′ polarization gradient but does not have a corresponding VTSS Hα filament (recall Figure 4). The nearby Hα filaments (Haffner et al. 1998) also lack counterparts in the 5′ polarization gradient. The polarization gradient highlights structures at particular angular scales (Herron et al. 2018), so more extended Hα structures (e.g., Haffner et al. 1998) may only be highlighted by the polarization gradient using a larger kernel. In contrast, some small-scale Hα structures do not have corresponding features in the polarization gradient. These ionized structures may not have significant LOS magnetic field strengths to induce an enhanced RM.

7. Summary and Conclusions

We present a multiphase analysis of the magnetized ISM in search of evidence that the high Galactic latitude magnetic field is shared between the ionized and neutral ISM. We visually compared structures in the 1.4 GHz GALFACTS polarization gradient to narrow, velocity-resolved GALFA-H I structures, focusing on those that are associated with diffuse/translucent H I emission and not spatially correlated with excess synchrotron emission. We identified a single region, G216 centered on $(\ell,\ b) \sim (216^\circ,\ +26^\circ)$, that contains coherent polarization gradient filaments clearly aligned with narrow H I structures. We compared multiphase observations and magnetic field tracers to investigate whether the ionized and neutral media of this region (1) are associated with one another and (2) share a common magnetic field.

This region is characterized by two filamentary structures in the polarization gradient that are roughly parallel to the Galactic plane. The polarization gradient filament farthest from the plane (F1) is spatially correlated with a bright Hα filament along the edge of a large, dusty H I cloud. The other filament (F2) is spatially correlated with the edges of very faint Hα emission and lies along the edge of a dusty H I filament.

We showed that the polarization gradient filaments are aligned with narrow H I structures over a $\sim 40\ {\rm km\ s}^{-1}$ H I velocity range using the RHT to identify coherent, linear structures. Using 3D RM synthesis, we showed that F1 may be a magnetically dominated ($B_\parallel = 6 \pm 4\ \mu$G, $\beta = 2.1^{+3.1}_{-2.1}$) filament with a magnetic field that is parallel to the filament. Since the 3D magnetic field geometry of F1 is unknown, this is an upper estimate of β based on $B_\parallel$ only. The alignment with narrow H I structures and dust polarization angles supports our interpretation of multiphase magnetic field alignment. The LOS and POS magnetic field orientations in the ionized and neutral gas, respectively, are both strongly coherent across the region. Our work is consistent with filamentary structures in the ISM being preferentially parallel to the Galactic plane along the mean magnetic field (e.g., Shajn 1958; Soler et al. 2020).

We used the Davis–Chandrasekhar–Fermi method to estimate the total magnetic field strength of $\sim 21\ \mu$G in the neutral medium using Planck dust polarization data. This is higher than the total magnetic field strength in the ionized gas inferred from our Faraday depth measurements ($B_{\rm tot} = 11 \pm 8\ \mu$G), suggesting an enhanced field strength in the neutral medium toward F1. We find two Zeeman splitting measurements along a single LOS toward the far east of our field (Heiles & Troland 2004) with magnetic field strengths of $-1.9 \pm 2.2\ \mu$G and $-3.2 \pm 3.7\ \mu$G. These Zeeman splitting measurements have the same LOS magnetic field direction as our Faraday depth measurement; however, more Zeeman splitting measurements are needed to make a statistically significant statement about a common LOS field direction between the ionized and neutral medium.

We discuss the lack of widespread alignments found between multiphase magnetic field tracers in the high Galactic latitude Arecibo sky. We find no strong evidence for an H I shell but are unable to rule out the possibility of a shock. We consider the possibility that G216 is associated with a short-timescale or physically rare phenomenon and suggest the possibility that a compressive event may have triggered the formation of a transient layer of dense ionized gas around a neutral gas cloud while aligning their respective magnetic fields. Further in-depth analyses on the alignment between

GALFACTS polarization gradient filaments and H I structures, or tracers of the ionized and neutral structures in general, are required to better understand the association between these phases of the magnetic ISM.

We are grateful to Peter Martin for helpful discussions, Josh Speagle for advice on 3D dust maps, and the anonymous referee for their kind and constructive comments that greatly improved our paper. J.L.C. acknowledges support from the Ontario Graduate Student Scholarship. J.L.C. and B.M.G. acknowledge the support of the Natural Sciences and Engineering Research Council of Canada (NSERC) through grant RGPIN-2015-05948 and of the Canada Research Chairs program. J.M.S. acknowledges the support of the Natural Sciences and Engineering Research Council of Canada (NSERC), 2019-04848. The Dunlap Institute is funded through an endowment established by the David Dunlap family and the University of Toronto. The University of Toronto operates on the traditional land of the Huron-Wendat, the Seneca, and, most recently, the Mississaugas of the Credit River; we are grateful to have the opportunity to work on this land.

This publication utilizes data from the Galactic ALFA H I (GALFA HI) survey data set obtained with the Arecibo L-band Feed Array (ALFA) on the Arecibo 305 m telescope. The Arecibo Observatory is operated by SRI International under a cooperative agreement with the National Science Foundation (AST-1100968) and in alliance with Ana G. Méndez-Universidad Metropolitana and the Universities Space Research Association. The GALFA H I surveys have been funded by the NSF through grants to Columbia University, the University of Wisconsin, and the University of California.

Software: Astropy (Astropy Collaboration et al. 2013, 2018), CARTA (Comrie et al. 2019), dustmaps (Green 2018), healpy (Zonca et al. 2019), matplotlib (Hunter 2007), numpy (Harris et al. 2020), RHT (Clark et al. 2014), RMTools (Purcell et al. 2020), scipy (Virtanen et al. 2020).

Appendix
RHT Backprojections

The RHT backprojections of the GALFA-H I data are shown in Figure A.1, and they reveal numerous H I structures across the entire field.

Figure A.2 shows the RHT backprojection of the 5′ GALFACTS polarization gradient. The RHT does exceptionally well at reconstructing the filamentary features in the polarization gradient, reproducing the single- and double-jump morphology of F1 along with the double- and triple-jump morphology of F2. Inspection of the RHT backprojection reveals that there are still signatures of scanning artifacts; however, they are $\sim$10 times fainter than the polarization gradient filaments.

Figure A.3 shows the RHT backprojection of the VTSS Hα emission.

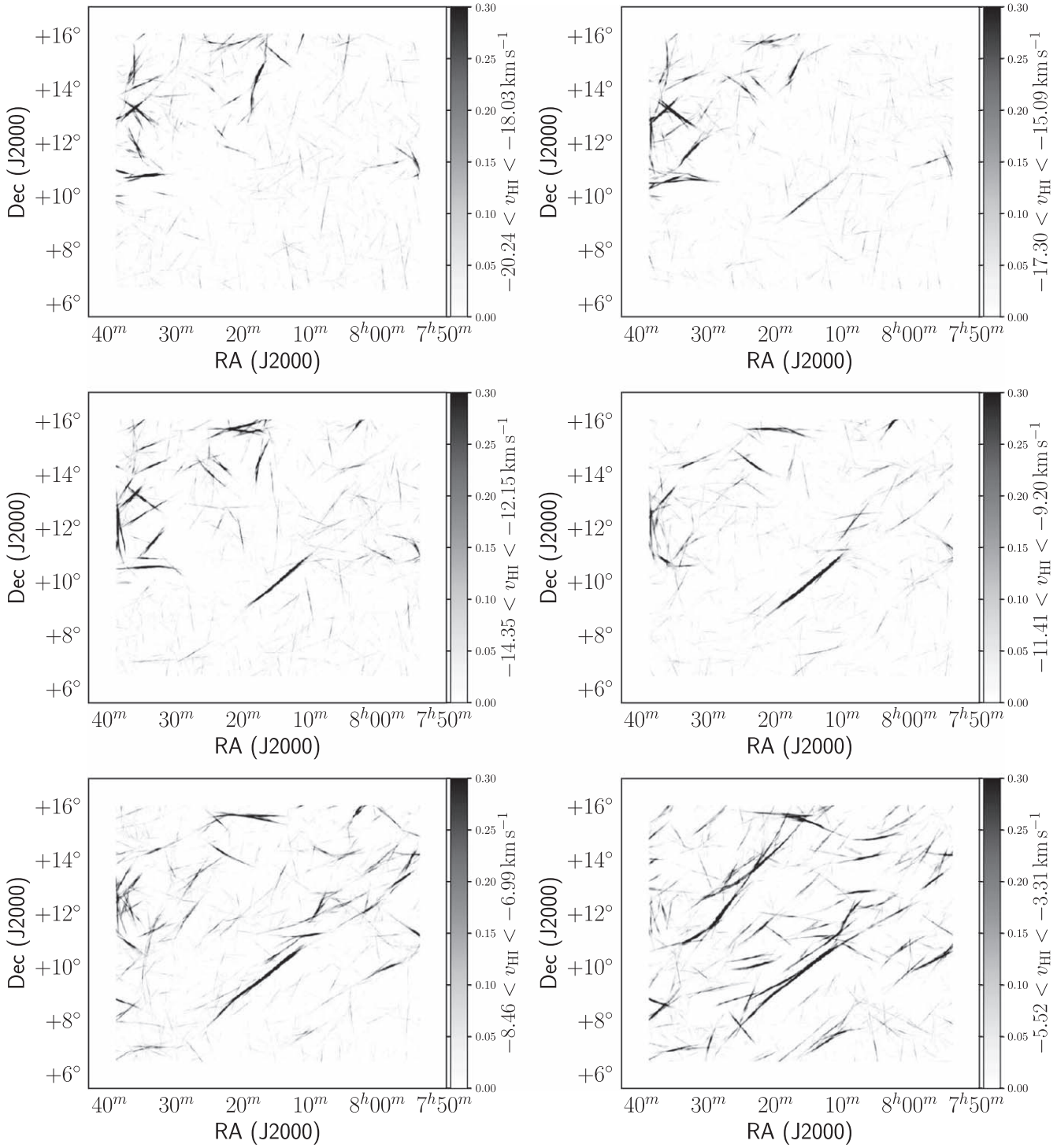

Figure A.1. (a) RHT backprojections for the GALFA-H I velocity slices within the range -20.24 km s$^{-1} < v_{\rm lsr} < -3.31$ km s^{-1}. (b) RHT backprojections for the GALFA-H I velocity slices within the range -2.58 km s$^{-1} < v_{\rm lsr} < 20.24$ km s^{-1}.

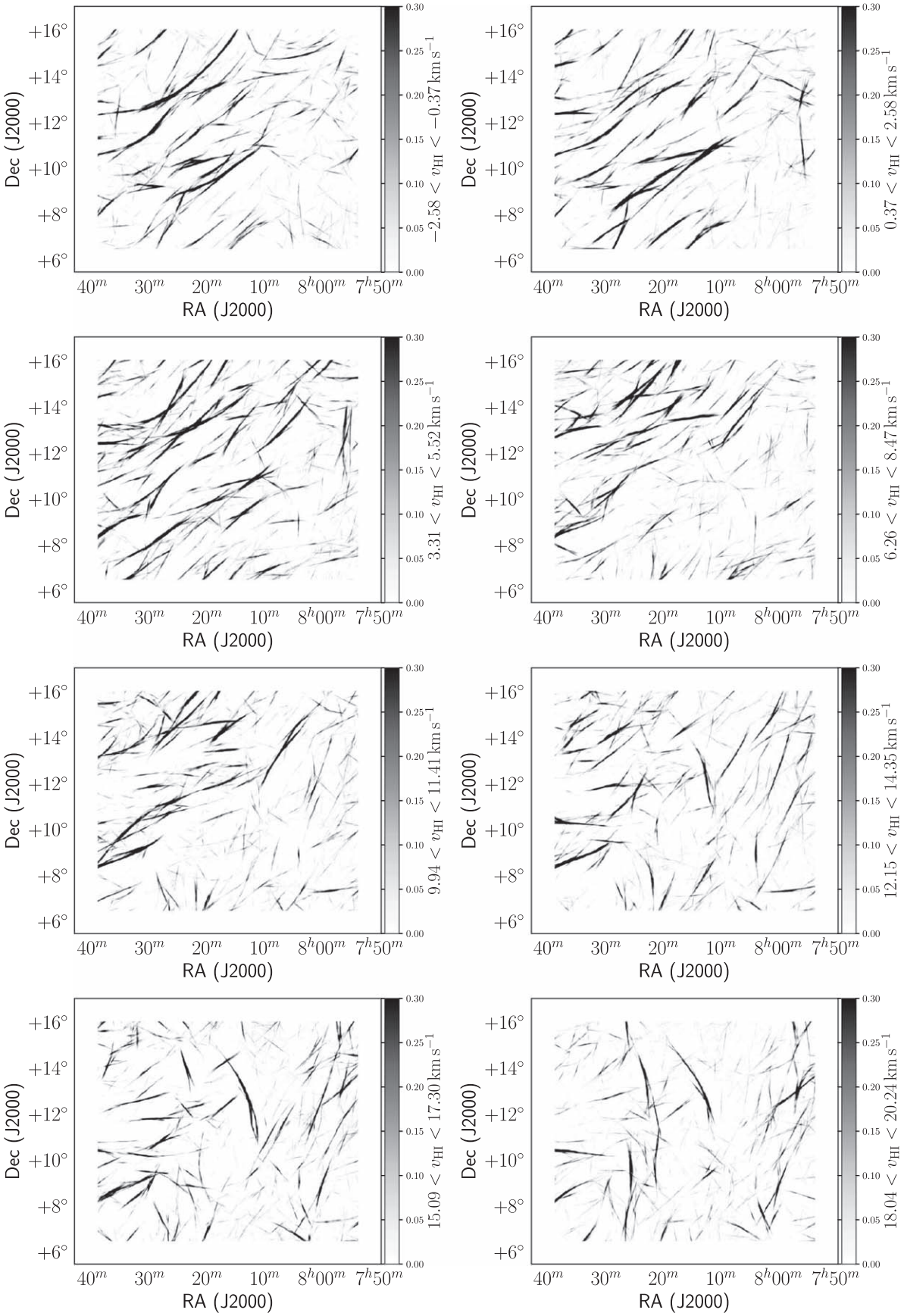

Figure A.1. (Continued.)

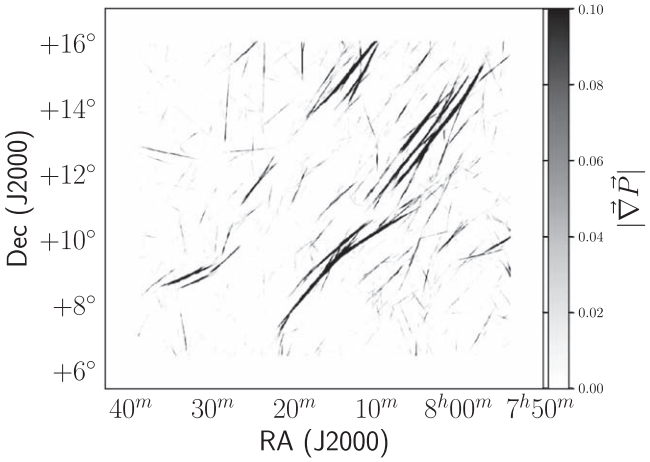

Figure A.2. RHT backprojection of the destriped 5′ GALFACTS $|\nabla P|_{\max}$ map.

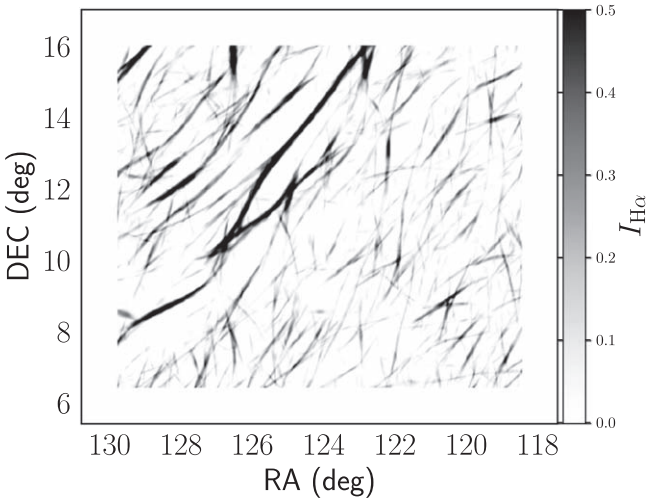

Figure A.3. RHT backprojection of the VTSS Hα map.

ORCID iDs

J. L. Campbell https://orcid.org/0000-0002-2511-5256
S. E. Clark https://orcid.org/0000-0002-7633-3376
B. M. Gaensler https://orcid.org/0000-0002-3382-9558
A. Marchal https://orcid.org/0000-0002-5501-232X
C. L. Van Eck https://orcid.org/0000-0002-7641-9946
A. A. Deshpande https://orcid.org/0000-0002-5146-2163
S. J. Gibson https://orcid.org/0000-0002-1495-760X
R. Ricci https://orcid.org/0000-0003-4631-1528
J. M. Stil https://orcid.org/0000-0003-2623-2064
A. R. Taylor https://orcid.org/0000-0001-9885-0676

References

Arnaud, K. A. 1996, in ASP Conf. Ser. 101, Astronomical Data Analysis Software and Systems V, ed. G. H. Jacoby & J. Barnes (San Francisco, CA: ASP), 17
Astropy Collaboration, Robitaille, T. P., Tollerud, E. J., et al. 2013, A&A, 558, A33
Astropy Collaboration, Price-Whelan, A. M., Sipőcz, P. M., et al. 2018, AJ, 156, 123
Berkhuijsen, E. M., Mitra, D., & Mueller, P. 2006, AN, 327, 82
Blagrave, K., Martin, P. G., Joncas, G., et al. 2017, ApJ, 834, 126
Bracco, A., Jelić, V., Marchal, A., et al. 2020, A&A, 644, L3
Brentjens, M. A., & de Bruyn, A. G. 2005, A&A, 441, 1217
Burkhart, B., Lazarian, A., & Gaensler, B. M. 2012, ApJ, 749, 145
Burn, B. J. 1966, MNRAS, 133, 67
Cabral, B., & Leedom, L. C. 1993, Proc. 20th Annual Conf. on Computer Graphics and Interactive Techniques, SIGGRAPH '93 (New York, NY: Association for Computing Machinery), 263
Calabretta, M. R., Staveley-Smith, L., & Barnes, D. G. 2014, PASA, 31, e007
Chambers, K. C., Magnier, E. A., Metcalfe, N., et al. 2016, arXiv:1612.05560
Chandrasekhar, S., & Fermi, E. 1953, ApJ, 118, 113
Cho, J., & Yoo, H. 2016, ApJ, 821, 21
Clark, S. E., Hill, J. C., Peek, J. E. G., Putman, M. E., & Babler, B. L. 2015, PhRvL, 115, 241302
Clark, S. E., Peek, J. E. G., & Miville-Deschênes, M. A. 2019, ApJ, 874, 171
Clark, S. E., Peek, J. E. G., & Putman, M. E. 2014, ApJ, 789, 82
Comrie, A., Wang, K.-S., Ford, P., et al. 2019, CARTA: The Cube Analysis and Rendering Tool for Astronomy, 1.2.0, Zenodo, doi:10.5281/zenodo.3403491
Crutcher, R. M., Wandelt, B., Heiles, C., Falgarone, E., & Troland, T. H. 2010, ApJ, 725, 466
Davis, L. 1951, PhRv, 81, 890
Dawson, J. R., McClure-Griffiths, N. M., Kawamura, A., et al. 2011, ApJ, 728, 127
Dennison, B., Simonetti, J. H., & Topasna, G. A. 1998, PASA, 15, 147
Ferrière, K. 2016, JPhCS, 767, 012006
Ferrière, K. 2020, PPCF, 62, 014014
Ferrière, K., West, J. L., & Jaffe, T. R. 2021, MNRAS, 507, 4968
Ferrière, K. M. 2001, RvMP, 73, 1031
Field, G. B., Goldsmith, D. W., & Habing, H. J. 1969, ApJL, 155, L149
Finkbeiner, D. P. 2003, ApJS, 146, 407
Gaensler, B. M., Dickey, J. M., McClure-Griffiths, N. M., et al. 2001, ApJ, 549, 959
Gaensler, B. M., Haverkorn, M., Burkhart, B., et al. 2011, Natur, 478, 214
Gaensler, B. M., Madsen, G. J., Chatterjee, S., & Mao, S. A. 2008, PASA, 25, 184
Gaustad, J. E., McCullough, P. R., Rosing, W., & Van Buren, D. 2001, PASP, 113, 1326
George, S. J., Stil, J. M., & Keller, B. W. 2012, PASA, 29, 214
Goldsmith, D. W., Habing, H. J., & Field, G. B. 1969, ApJ, 158, 173
Gray, A. D., Landecker, T. L., Dewdney, P. E., & Taylor, A. R. 1998, Natur, 393, 660
Green, G. 2018, JOSS, 3, 695
Green, G. M., Schlafly, E., Zucker, C., Speagle, J. S., & Finkbeiner, D. 2019, ApJ, 887, 93
Green, J. A., McClure-Griffiths, N. M., Caswell, J. L., Robishaw, T., & Harvey-Smith, L. 2012, MNRAS, 425, 2530
Guram, S. S., Andrecut, M., George, S. J., & Taylor, A. R. 2011, in ASP Conf. Ser. 442, Astronomical Data Analysis Software and Systems XX, ed. I. N. Evans et al. (San Francisco, CA: ASP), 317
Guram, S. S., & Taylor, A. R. 2009, in ASP Conf. Ser. 407, The Galactic ALFA Continuum Transit Survey: GALFACTS, ed. D. J. Saikia et al. (San Francisco, CA: ASP), 282
Haffner, L. M., Dettmar, R. J., Beckman, J. E., et al. 2009, RvMP, 81, 969
Haffner, L. M., Reynolds, R. J., & Tufte, S. L. 1998, ApJL, 501, L83
Haffner, L. M., Reynolds, R. J., Tufte, S. L., et al. 2003, ApJS, 149, 405
Harris, C. R., Millman, K. J., van der Walt, S. J., et al. 2020, Natur, 585, 357
Haverkorn, M., Boulanger, F., Enßlin, T., et al. 2019, Galax, 7, 17
Haverkorn, M., & Heitsch, F. 2004, A&A, 421, 1011
Haverkorn, M., Katgert, P., & de Bruyn, A. G. 2003a, A&A, 403, 1031
Haverkorn, M., Katgert, P., & de Bruyn, A. G. 2003b, A&A, 404, 233
Haverkorn, M., Katgert, P., & de Bruyn, A. G. 2004a, A&A, 427, 169
Haverkorn, M., Katgert, P., & de Bruyn, A. G. 2004b, A&A, 427, 549
Heald, G., Braun, R., & Edmonds, R. 2009, A&A, 503, 409
Heiles, C. 1967, ApJS, 15, 97
Heiles, C. 1979, ApJ, 229, 533
Heiles, C. 1984, ApJS, 55, 585
Heiles, C., & Haverkorn, M. 2012, SSRv, 166, 293
Heiles, C., & Troland, T. H. 2003, ApJ, 586, 1067
Heiles, C., & Troland, T. H. 2004, ApJS, 151, 271
Heitsch, F., Zweibel, E. G., Mac Low, M.-M., Li, P., & Norman, M. L. 2001, ApJ, 561, 800
Herron, C. A., Gaensler, B. M., Lewis, G. F., & McClure-Griffiths, N. M. 2018, ApJ, 853, 9
HI4PI Collaboration, Ben Bekhti, N., Flöer, L., et al. 2016, A&A, 594, A116
Hill, A. 2018, Galax, 6, 129
Hill, A. S., Benjamin, R. A., Kowal, G., et al. 2008, ApJ, 686, 363

Hill, A. S., Landecker, T. L., Carretti, E., et al. 2017, MNRAS, 467, 4631
Hu, E. M. 1981, ApJ, 248, 119
Hunter, J. D. 2007, CSE, 9, 90
Iacobelli, M., Burkhart, B., Haverkorn, M., et al. 2014, A&A, 566, A5
Jaffe, T. R. 2019, Galax, 7, 52
Jaffe, T. R., Leahy, J. P., Banday, A. J., et al. 2010, MNRAS, 401, 1013
Jelić, V., de Bruyn, A. G., Pandey, V. N., et al. 2015, A&A, 583, A137
Jelić, V., Prelogović, D., Haverkorn, M., Remeijn, J., & Klindžić, D. 2018, A&A, 615, L3
Kado-Fong, E., Kim, J.-G., Ostriker, E. C., & Kim, C.-G. 2020, ApJ, 897, 143
Kalberla, P. M. W., & Haud, U. 2015, A&A, 578, A78
Kalberla, P. M. W., & Haud, U. 2020, arXiv:2003.01454
Kalberla, P. M. W., & Kerp, J. 2016, A&A, 595, A37
Kalberla, P. M. W., Kerp, J., Haud, U., & Haverkorn, M. 2017, A&A, 607, A15
Kalberla, P. M. W., Kerp, J., Haud, U., et al. 2016, ApJ, 821, 117
Kalberla, P. M. W., McClure-Griffiths, N. M., Pisano, D. J., et al. 2010, A&A, 521, A17
Kanekar, N., Subrahmanyan, R., Chengalur, J. N., & Safouris, V. 2003, MNRAS, 346, L57
Kim, C.-G., & Ostriker, E. C. 2018, ApJ, 853, 173
Lallement, R., Babusiaux, C., Vergely, J. L., et al. 2019, A&A, 625, A135
Lazarian, A., & Yuen, K. H. 2018, ApJ, 853, 96
Leahy, P. 2018, in GALFACTS Internal Memo, 1
Marchal, A., & Miville-Deschênes, M.-A. 2021, ApJ, 908, 186
Marchal, A., Miville-Deschênes, M.-A., Orieux, F., et al. 2019, A&A, 626, A101
Martin, P. G., Blagrave, K. P. M., Lockman, F. J., et al. 2015, ApJ, 809, 153
McClure-Griffiths, N. M., Dickey, J. M., Gaensler, B. M., & Green, A. J. 2002, ApJ, 578, 176
McClure-Griffiths, N. M., Dickey, J. M., Gaensler, B. M., & Green, A. J. 2003, ApJ, 594, 833
McClure-Griffiths, N. M., Dickey, J. M., Gaensler, B. M., Green, A. J., & Haverkorn, M. 2006, ApJ, 652, 1339
McClure-Griffiths, N. M., Pisano, D. J., Calabretta, M. R., et al. 2009, ApJS, 181, 398
McKee, C. F., & Ostriker, J. P. 1977, ApJ, 218, 148
Murray, C. E., Stanimirović, S., Goss, W. M., et al. 2015, ApJ, 804, 89
Murray, C. E., Stanimirović, S., Goss, W. M., et al. 2018, ApJS, 238, 14
Nota, T., & Katgert, P. 2010, A&A, 513, A65
Ogbodo, C. S., Green, J. A., Dawson, J. R., et al. 2020, MNRAS, 493, 199
Peek, J. E. G., Babler, B. L., Zheng, Y., et al. 2018, ApJS, 234, 2
Peek, J. E. G., & Clark, S. E. 2019, ApJL, 886, L13
Planck Collaboration, Abergel, A., Ade, P. A. R., et al. 2014, A&A, 571, A11
Planck Collaboration, Adam, R., Ade, P. A. R., et al. 2016, A&A, 594, A8
Planck Collaboration, Aghanim, N., Akrami, Y., et al. 2020a, A&A, 641, A3
Planck Collaboration, Aghanim, N., Akrami, Y., et al. 2020b, A&A, 641, A12
Purcell, C. R., Van Eck, C. L., West, J., Sun, X. H., & Gaensler, B. M. 2020, RM-Tools: Rotation measure (RM) synthesis and Stokes QU-fitting, Astrophysics Source Code Library, ascl:2005.003
Rand, R. J., & Kulkarni, S. R. 1989, ApJ, 343, 760
Reid, M. J., Menten, K. M., Brunthaler, A., et al. 2014, ApJ, 783, 130
Reynolds, R. J. 1990a, in IAU Symp. 139, The Galactic and Extragalactic Background Radiation, ed. S. Bowyer & C. Leinert (Dordrecht: Kluwer), 157
Reynolds, R. J. 1984, ApJ, 282, 191
Reynolds, R. J. 1988, ApJ, 333, 341
Reynolds, R. J. 1990b, ApJ, 348, 153
Reynolds, R. J. 1990c, ApJL, 349, L17
Robishaw, T., & Heiles, C. 2021, in The WSPC Handbook of Astronomical Instrumentation, ed. A. Wolszczan (State College, PA: World Scientific), 127
Robitaille, J. F., & Scaife, A. M. M. 2015, MNRAS, 451, 372
Roy, N., Kanekar, N., & Chengalur, J. N. 2013, MNRAS, 436, 2366
Saury, E., Miville-Deschênes, M. A., Hennebelle, P., Audit, E., & Schmidt, W. 2014, A&A, 567, A16
Schlafly, E. F., Meisner, A. M., Stutz, A. M., et al. 2016, ApJ, 821, 78
Schlegel, D. J., Finkbeiner, D. P., & Davis, M. 1998, ApJ, 500, 525
Schnitzeler, D. H. F. M., Katgert, P., & de Bruyn, A. G. 2009, A&A, 494, 611
Shajn, G. A. 1958, in IAU Symp. 6, Electromagnetic Phenomena in Cosmical Physics, ed. B. Lehnert (Cambridge: Cambridge Univ. Press), 182
Shimwell, T. W., Röttgering, H. J. A., Best, P. N., et al. 2017, A&A, 598, A104
Skalidis, R., Sternberg, J., Beattie, J. R., Pavlidou, V., & Tassis, K. 2021, A&A, 656, A118
Skrutskie, M. F., Cutri, R. M., Stiening, R., et al. 2006, AJ, 131, 1163
Snowden, S. L., Egger, R., Freyberg, M. J., et al. 1997, ApJ, 485, 125
Soler, J. D., Beuther, H., Syed, J., et al. 2020, A&A, 642, A163
Soler, J. D., Bracco, A., & Pon, A. 2018, A&A, 609, L3
Stil, J. M., & Hryhoriw, A. 2016, ApJ, 826, 202
Sun, X. H., Reich, W., Waelkens, A., & Enßlin, T. A. 2008, A&A, 477, 573
Tahani, M., Plume, R., Brown, J. C., & Kainulainen, J. 2018, A&A, 614, A100
Taylor, A. R. 2012, in GALFACTS Internal Note, 1
Taylor, A. R. 2013, IOP Conf. Ser.: Mater. Sci. Eng., 44, 012019
Taylor, A. R., & Salter, C. J. 2010, in ASP Conf. Ser., 438, GALFACTS: The G-ALFA Continuum Transit Survey, ed. R. Kothes, T. L. Landecker, & A. G. Willis (San Francisco, CA: ASP), 402
Taylor, A. R., Stil, J. M., & Sunstrum, C. 2009, ApJ, 702, 1230
Thomson, A. J. M., Landecker, T. L., Dickey, J. M., et al. 2019, MNRAS, 487, 4751
Tritsis, A., Federrath, C., & Pavlidou, V. 2019, ApJ, 873, 38
Turić, L., Jelić, V., Jaspers, R., et al. 2021, A&A, 654, A5
Uyaniker, B., Landecker, T. L., Gray, A. D., & Kothes, R. 2003, ApJ, 585, 785
van de Hulst, H. C. 1967, ARA&A, 5, 167
Van Eck, C. L., Haverkorn, M., Alves, M. I. R., et al. 2017, A&A, 597, A98
Van Eck, C. L., Haverkorn, M., Alves, M. I. R., et al. 2019, A&A, 623, A71
van Haarlem, M. P., Wise, M. W., Gunst, A. W., et al. 2013, A&A, 556, A2
Verschuur, G. L. 1970, AJ, 75, 687
Virtanen, P., Gommers, R., Burovski, E., et al. 2020, scipy/scipy: SciPy 1.5.3, v1.5.3, Zenodo, doi:10.5281/zenodo.595738
Weisberg, J. M., Stanimirović, S., Xilouris, K., et al. 2008, ApJ, 674, 286
Wenger, T. V., Balser, D. S., Anderson, L. D., & Bania, T. M. 2018, ApJ, 856, 52
Wieringa, M. H., de Bruyn, A. G., Jansen, D., Brouw, W. N., & Katgert, P. 1993, A&A, 268, 215
Winkel, B., Kerp, J., Flöer, L., et al. 2016, A&A, 585, A41
Wolfire, M. G., McKee, C. F., Hollenbach, D., & Tielens, A. G. G. M. 2003, ApJ, 587, 278
Wolleben, M., Landecker, T. L., Carretti, E., et al. 2009, in IAU Symp. 259, Cosmic Magnetic Fields: From Planets, to Stars and Galaxies, ed. K. G. Strassmeier, A. G. Kosovichev, & J. E. Beckman (Cambridge: Cambridge Univ. Press), 89
Wolleben, M., Landecker, T. L., Reich, W., & Wielebinski, R. 2006, A&A, 448, 411
Wood, K., Hill, A. S., Joung, M. R., et al. 2010, ApJ, 721, 1397
Yoon, H., & Cho, J. 2019, ApJ, 880, 137
Zaroubi, S., Jelic, V., de Bruyn, A. G., et al. 2015, MNRAS, 454, L46
Zonca, A., Singer, L., Lenz, D., et al. 2019, JOSS, 4, 1298